THE DEFECT ENERGIES AND DEFORMATION MECHANISMS OF SINGLE CRYSTAL SUPERALLOYS

by

Graham Stewart Hillier, B.Met.

St. John's College
Cambridge

A dissertation submitted for the degree of Philosophiae Doctor at the University of Cambridge

September 1984

Dedicated to my Mum and Dad

PREFACE

This dissertation describes work carried out in the Department of Metallurgy and Materials Science, Cambridge between October 1981 and September 1984 under the supervision of Dr. H.K.D.H. Bhadeshia.

The contents are, to the best of my knowledge, original except where acknowledgement has been made to the work of others, and the work has been carried out without collaboration. This dissertation contains less than 60,000 words and no part of it has been, or is being, submitted for any other degree, diploma or qualification at any other university.

Graham Hillier

G.S. Hillier
St. John's College
September 1984

Acknowledgements

I am grateful to Dr. H.K.D.H. Bhadeshia for his advice and assistance throughout my project. I am especially indebted to Dr. Cathy Rae for many stimulating and fruitful discussions, and I would also like to thank Dr. W.M. Stobbs for his help with electron microscopical techniques. Thanks are also due to Mr. R.G. Roome and Mr. P. Doorbar for allowing me to use the JEOL 200 CX at Rolls-Royce, and for their advice on the use of TEM to study superalloy materials.

The cast single crystal superalloys were supplied by Rolls-Royce Ltd., Derby. I wish to thank Dr. R.P. Arthey and Mrs J. Hooker for looking after alloy manufacture and making stress-rupture test facilities available. In addition I wish to thank Mrs. Janet Laing for her excellent typing of this thesis, and also the technical staff, both in the department and at Rolls-Royce, for their help.

Thanks are also due to Professor R.W.K. Honeycombe, F.R.S., for the provision of laboratory facilities, and the SERC for the provision of a quota award to support this work.

Finally, I would like to thank my Mum, Dad and sister, Jacqui, for their interest and encouragement over the last three years.

The Defect Energies and Deformation Mechanisms of Single Crystal Superalloys

G.S. Hillier

Summary

The homogenisation behaviour of seven cast single crystal Ni-base superalloys with Ti contents between 1.8 and 2.7at.% has been studied using various microanalytical techniques. It is found that homogenisation for 32 hrs at 1570K is sufficient to produce reasonably uniform alloys. The γ' precipitate has been coarsened by treating the specimens for 16 hrs at 1300K and it is found that there is no perceptible change in γ/γ' misfit or composition of the specimens before and after growth.

Bright field and weak beam dark field transmission electron microscopy are used extensively to study some of the dislocation interactions in the γ' of three of the alloys after deformation at room temperature and annealing at 1170K. Hexagonal and square superdislocation networks are studied and mechanisms are proposed for the creation of such defects.

Superdislocation spacings have been measured in order to deduce the variation in the antiphase boundary (APB) energy of three of the alloys as a function of Ti content. A new technique for the evaluation of superlattice stacking fault (SSF) energy from three-fold supernode configurations is presented and used to study the dependence of SSF energy on Ti content. It seems that APB energy is essentially independent of Ti but that the intrinsic and extrinsic SSF energies decrease with increasing Ti. It is suggested that the decrease in the SSF energies is due to the stabilization of SSFs by Ti segregating to the planar faults. Such stabilization is expected since the faults involve a stacking sequence equivalent to a few layers of the Ni_3Ti structure.

A modification is proposed to the accepted superalloy deformation mechanisms by γ' shear as a result of the measured energy values. This involves a mechanism, similar to Suzuki locking, which retards γ' shearing by the passage of partial dislocations.

CONTENTS

ABBREVIATIONS AND SYMBOLS

APB - Anti-phase boundary

FCC - Face centred cubic

FIM - Field ion microscope

SSF - Superlattice stacking fault

SESF - Superlattice extrinsic stacking fault

SISF - Superlattice intrinsic stacking fault

TEM - Transmission electron microscope

γ - Gamma matrix

γ' - Gamma prime precipitate

A - Anisotropy factor

a - Lattice parameter

$\underline{B}$ - Electron beam direction

$\underline{b}$ - Dislocation Burgers vector

c_{ij} - Elastic constants

c_x - Concentration of element x

D_x - Diffusion coefficient of element x

d - Diffusion distance

F - Force

$G(\rho)$ - Geometric function of supernode

$\underline{g}$ - Diffraction vector

M - γ/γ' misfit

m - Apparent dislocation spacing

$\underline{N}$ - APB plane normal

$\underline{R}$ - Lattice displacement vector

R - Internal dimension of supernode

r - Distance from dislocation

- True superdislocation spacing

$\underline{s}$ - Deviation from the Bragg condition

T - Temperature

T_m - Melting point

t - Time

$\underline{u}$ - Dislocation line vector

v - Velocity

$W_{(n\underline{g},n\underline{g})}$ - Weak beam dark field condition

X - Distance

X, Y, Z - Co-ordinate axes

x_j, y_j, z_j - Co-ordinate axes of dislocation j

z - Distance

α - Phase factor

γ_A - Anti-phase boundary energy

γ_{SSF} - Superlattice stacking fault energy

$\dot{\varepsilon}$ - Secondary creep strain rate

θ - Angle between dislocation line vector and Burgers vector

- Angle between dislocation spacing vector and electron beam direction

λ - Wavelength

μ - Isotropic shear modulus: equivalent to $[C_{44}(C_{11}-C_{12})/2]^2$ for screw dislocations

ν - Poissons ratio

$\xi_{\underline{g}}$ - Extinction distance

ρ - Dislocation density

- $\frac{\text{True superdislocation spacing}}{\text{Internal dimension of supernode}} = \frac{r}{R}$

σ_j - Stress on a dislocation

Φ - Angular co-ordinate

ϕ - Wave amplitude

$\underline{\omega}$ - Deviation parameter ($=\underline{s}.\xi_{\underline{g}}$)

CHAPTER 1

BACKGROUND AND INTRODUCTION

1.1 The Principles of Jet Propulsion and the Working Cycle of the Gas Turbine Engine

The possibility of using the jet principle to move an aircraft through the air had interested aircraft designers for a long period but the inability of piston engines with propellers to provide the large airflows necessary to produce a 'jet' caused serious problems. In 1930 Frank Whittle was granted a patent to apply the gas turbine to jet propulsion (Whittle, 1930). Eleven years later his engine completed its first flight. Since that time gas turbine engines have been extensively developed until they have become vitally important in applications which require very high power outputs from compact power sources, particularly in the aircraft and ship industries. Recently they have also been used industrially for pumping natural gas across continents and for small scale power generation in isolated areas away from normal energy supplies.

The principal of jet propulsion is an application of Sir Isaac Newton's third law of motion which states that 'for every force acting on a body there is an equal and opposite reaction'. The earliest known example of the jet engine was produced in about A.D. 100 by the famous mechanician Hero of Alexandria (see Bernal, 1969). This engine showed how the momentum of steam issuing from a jet could cause the 'engine' to revolve by producing an equal and opposite reaction (fig. 1.1). For aircraft propulsion the fluid forming the jet is air, rather than steam. As in Hero's engine the expansion of the accelerated air has an equal and opposite effect on the engine; thus, providing propulsive power which causes the engine and the

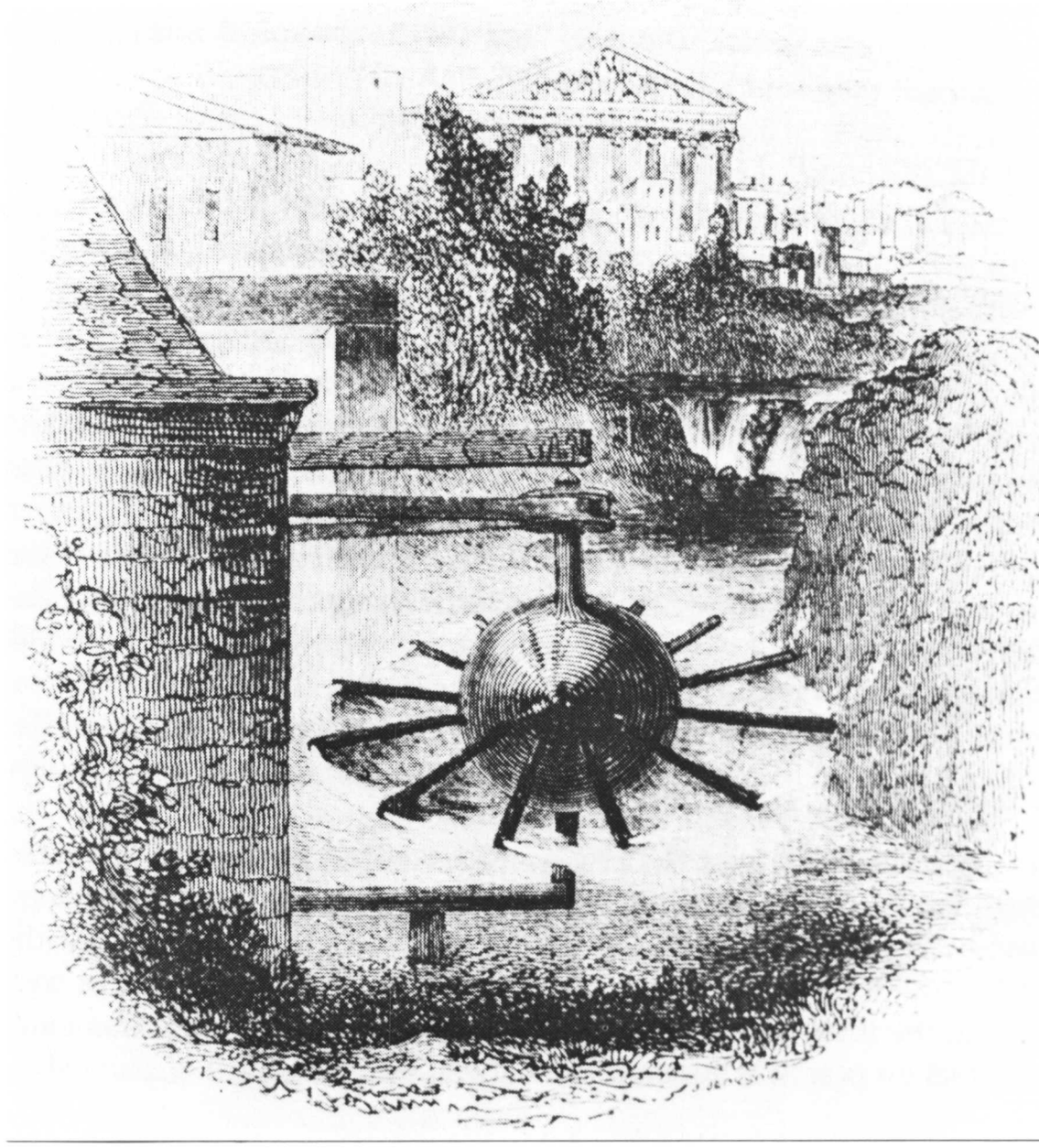

Fig. 1.1. A reproduction of the aeolipyle more commonly known as Hero's engine. The drawing is from a book by Dionysius Lardner, published in 1856, in which the principles of steam as a motive power are discussed. (Bernal, 1969.)

aircraft to which it is attached to move forward.

A section through the original Whittle engine is shown together with sections through two other more modern aircraft gas turbines in fig. 1.2. All three engines work on the same continuous induction, compression, combustion and exhaust cycle. The continuous cycle and absence of reciprocating parts gives a smooth running engine which enables higher power outputs to be gained from gas turbines, when compared with piston engines of the same size. A schematic diagram showing the working cycle of the gas turbine is shown in fig. 1.3. From A to B ambient air is compressed several times by the compressor section (fig. 1.4). From B to C it is heated in the combustion chamber by the injection of burning fuel; this causes a large increase in gas volume. From C to D the expanding gases flow through the turbine and jet pipe before being returned to the atmosphere. During the final part of the cycle some of the energy in the gas is turned into mechanical power by the turbine and this is used to maintain engine operation by driving the compressor; the rest of the gas stream provides propulsive power as it is discharged to the atmosphere. Figure 1.4 shows the typical air flow through a single-shaft axial flow turbo-jet.

Modern jet engines such as the R.B.211 (fig. 1.2c) split the air-flow through the engine into two. Eighty per cent of the air is accelerated a little by the large front fan acting as a large propeller. This air is ducted out past the engine core. The 'fan' is driven by the low pressure compressor which is sited at the back of the exhaust air stream from the engine core. The other 20% of the airflow passes through the engine core. The compressor and turbine assembly is split into two, an intermediate pressure section and a high pressure section. These are totally independent from one another and can rotate at different speeds. This enables significant gains to be made in the propulsive and specific fuel efficiencies of the engine. Turbo-fan and turbo-jet engines in aircraft have their power

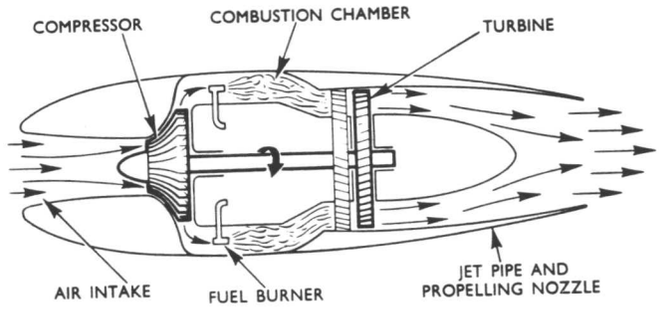

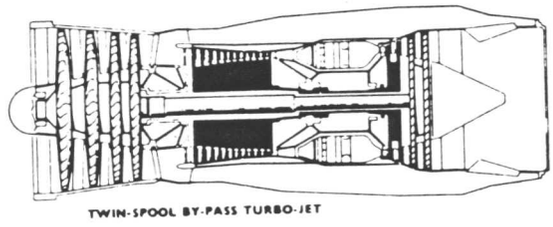

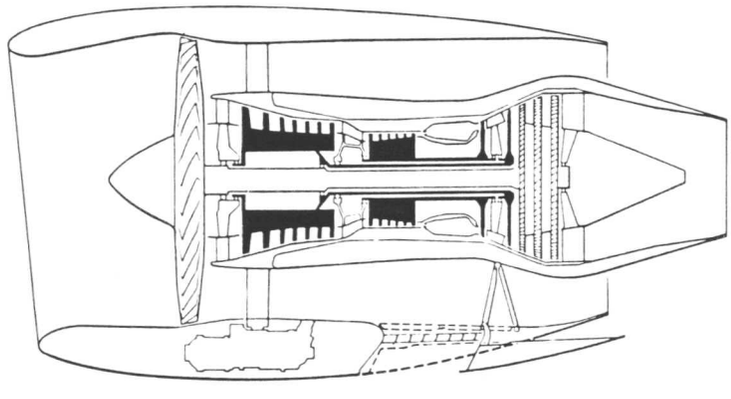

Fig. 1.2. Diagrams showing the mechanical arrangement of three typical gas turbines. The arrangements shown are (a) the single-spool Whittle engine, (b) the Rolls-Royce Spey twin-spool by-pass turbo-jet, and (c) the Rolls-Royce RB211 three shaft by-pass turbo-fan. (From The Jet Engine, 1973 and Driver, Hall and Meetham, 1981.)

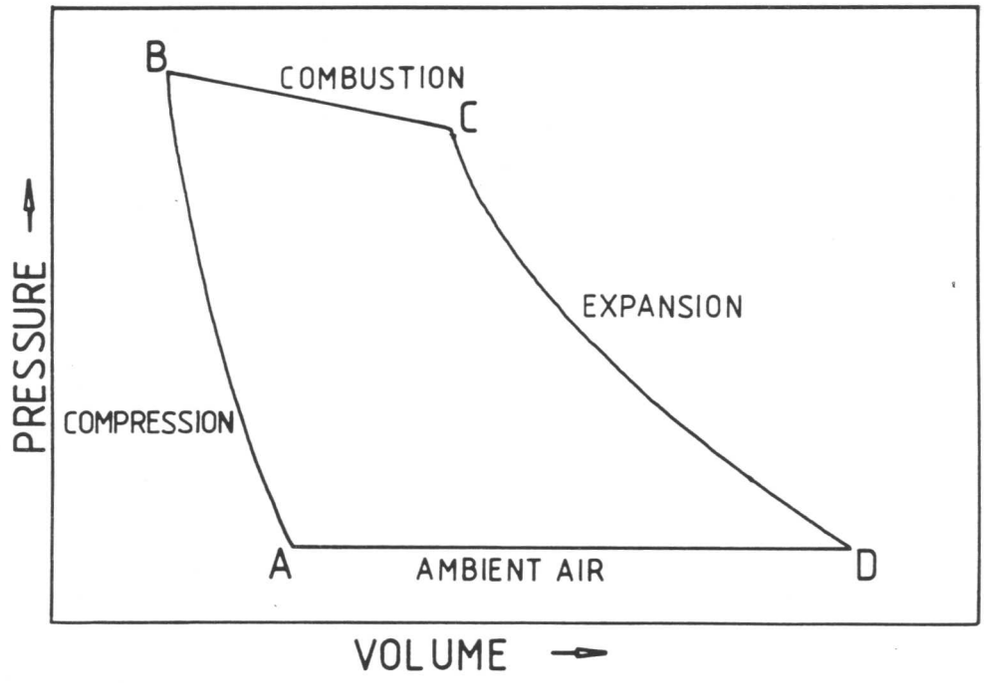

Fig. 1.3. The working cycle of the gas turbine on a pressure-volume diagram (The Jet Engine, 1973).

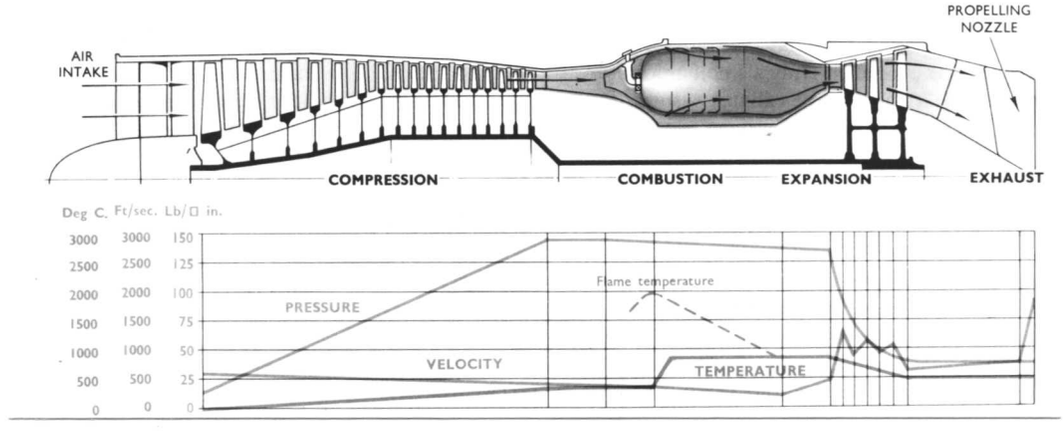

Fig. 1.4. The airflow through a typical single-spool axial flow turbo-jet engine (The Jet Engine, 1973).

ratings expressed in lbs thrust, the thrust being the force exerted by the expansion of the accelerated air on the engine after the turbines have taken their share. (The R.B.211 generates between 37,400 and 56,000 lbs thrust at sea level.) Propeller, ship and industrial gas turbines transfer power to rotate a shaft via a reduction gear. This is done by installing more turbine stages; these extract most of the energy from the exhaust gas stream and transfer it to the rotating shaft. The power output is expressed in shaft horse power. The operation of the gas turbine and detailed information about the various engine sections and assemblies mentioned above can be found in The Jet Engine (1973).

The rising cost of fuel has meant that gas turbine manufacturers have to produce increasingly efficient engines. The efficiency of any heat engine is improved by increasing the difference between the maximum and minimum temperatures of the heat cycle. The ambient temperature of the air is fixed, therefore any improvement in efficiency requires an increase in the temperature of the hot gases entering the turbine. The other major factor affecting efficiency is the compression ratio. Figure 1.5 shows the effect of compression ratio and turbine entry temperature (TET) on the specific fuel efficiency and specific thrust. It is shown that for an efficient high thrust gas turbine a high compression ratio and a high TET are required. The TET is limited by the maximum operating temperature of the materials in the turbine assembly. Consequently the major materials research effort in the gas turbine industry is directed towards improving the temperature capability of the first stage turbine blade and disc materials.

1.2 Turbine Blade Material Requirements

The high pressure turbine blades operate under the most arduous condition in the gas turbine engine. Not only do they experience gas temperatures in excess of 1500K and stresses of up to 550 MPa, which can

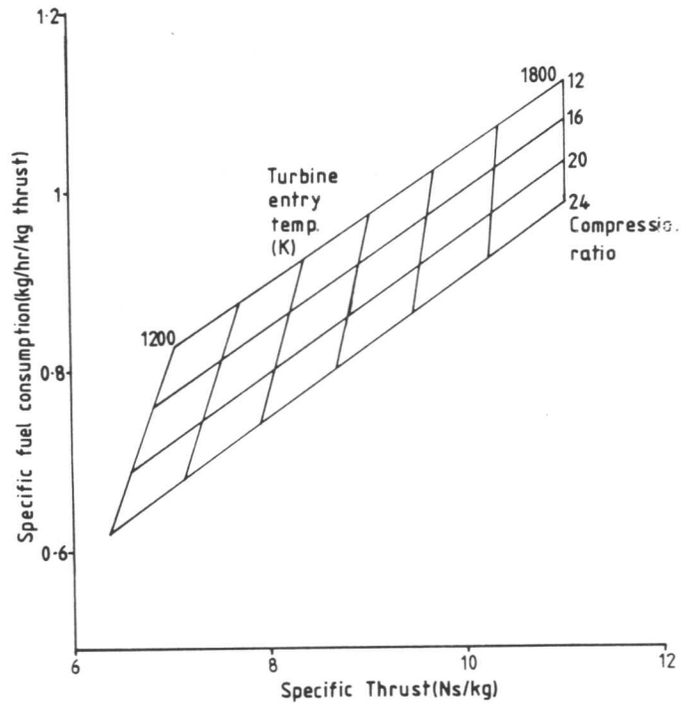

Fig. 1.5. The effect of turbine entry temperature and compression ratio on specific thrust and specific fuel consumption. (Driver et al., 1981.)

cause creep, but they also experience thermal fatigue due to temperature transients on take-off and landing. The blades are surrounded by highly oxidising gases which may contain contaminents such as chlorides and sulphates; these can cause hot corrosion. Blades may also suffer erosion by sand ingested on take-off, from the atmosphere (particles are present at up to 30,000 ft. over the world's deserts), or by particles of carbon formed during the combustion process. Creep and thermal fatigue can alter the turbine vibration characteristics so much that a resonant frequency is reached causing high cycle fatigue. This may, in time, cause a blade or part of a blade to break off in the engine where it will come into contact with other blades. The turbine assembly must, therefore, be impact resistant if disintegration of the engine is to be prevented.

To sum up, turbine blades must have high (>1200K) and intermediate (1000-1200K) temperature creep resistance; to a lesser degree they must be resistant to oxidation and hot corrosion, erosion, thermal fatigue and impact. In addition to this, to be economic, they must have service lives in excess of 7000 hrs. and be fairly easy to fabricate.

1.3 Material Choice

Austenitic stainless steel was used for the turbine blading in the first Whittle engine but this proved to have insufficient creep resistance and was soon replaced by the first two members of the 'Nimonic' series, alloys 75 and 80 (table 1.1). Since then most aircraft high pressure gas turbine blading has been made from nickel-base superalloys. Cobalt, iron and chromium-based alloys have been tried but the Ni-base group has been by far the most successful; only these will be subsequently discussed.

Successively more complex alloys have been empirically developed over the years resulting in modern polycrystalline superalloys such as Mar-M 002 and Mar-M 200 (table 1.1).

Table 1.1. Some Common Superalloy Compositions (at.%)

	Alloy				
Element	Nimonic 75	Nimonic 80A	Mar-M 002	Mar-M 200	SRR 99
Ni	76.0	70.7	60.5	59.5	66.5
Al	-	2.7	12.2	11.2	12.1
Ti	0.5	2.9	1.9	2.5	2.7
Cr	21.8	20.8	10.2	10.4	9.7
Co	-	1.1	10.0	10.2	4.6
W	-	-	3.2	4.1	3.0
Ta	-	-	0.8	-	0.9
Nb	-	-	-	0.7	-
Mn	0.1	0.1	-	-	-
Si	1.4	1.4	-	-	-
C	0.3	0.3	0.7	0.7	<0.1
B	-	-	-	0.1	-
Zr	-	-	∿0.03	∿0.03	-
Hf	-	-	0.5	0.7	-

Table 1.2. Bulk Compositions of the Alloys Studied (at.%)

	Alloy						
Element	A	B	C	D	E	F	G
Ni	67.7	68.2	67.8	68.2	68.3	68.1	68.9
Al	11.8	11.4	12.0	11.9	11.8	11.8	11.9
Ti	2.7	2.5	2.4	2.2	2.1	2.1	1.8
Cr	9.3	9.4	9.3	9.3	9.4	9.4	9.3
Co	4.8	4.8	4.8	4.7	4.8	4.8	4.8
Ta	0.9	0.9	0.9	0.9	0.9	0.9	0.9
W	2.8	2.8	2.8	2.8	2.8	2.8	2.8

These alloys are based on a Ni-Cr solid solution similar to that patented by Marsh (1906) for electrical heating elements. This heat resistant FCC matrix, γ, is strengthened by the precipitation of a high volume fraction of the $L1_2$ ordered precipitate gamma prime, γ' (fig. 4.3a). Gamma prime, chemical formula Ni_3Al, can be strengthened by additions of Ti, Ta and Nb while γ can be strengthened by Co and W. Zr and Hf can be added with C and B to strengthen the grain boundaries by the precipitation of small globular carbides and borides on the boundaries. Cr and Al also provide some corrosion protection by forming oxide films on the surface. Operating conditions are now exceeding the level of protection offered by these films and specific corrosion resistant coatings have been developed. A discussion of these is outside the scope of this thesis; a good review is that by Restall (1981).

In the late 1960's and early 1970's the rush to produce compositionally more complex alloys was reversed by the development of a process to produce single crystal turbine blades. These require no grain boundary strengthening so the alloy composition is more simple (eg. SRR99, table 1.1); they also have superior mechanical properties. The process developments leading to single crystal growth are discussed below.

1.4 Process Developments

1.4.1 Forging

In the early days of gas turbine development all turbine blades were drop-forged. This process soon gave way to press forging which enabled better control of the blade microstructure. Most low temperature, low pressure turbine blades are still manufactured by a forging route, some are manufactured by a combination of extrustion and forging processes. For an account of turbine blade forging see Wells (1981).

Greater property demands from engine designers forced the alloy manufacturers to increase the γ' content of wrought alloys. This decreased

the solidus and liquidus temperatures but increased the solid solution temperature resulting in a considerable narrowing of the hot working range. Further problems arose with the introduction of air-cooled blades where the aerofoil contains intricate internal passages (see fig. 1.6) which carry cooler air to lower the blade surface temperature. The advantage gained by using cooled blades is that they can operate at higher TETs and propulsive efficiency is improved for a given material. It proved extremely difficult to successfully manufacture complex cooled blades from high strength superalloys using extrusion and forging.

An alternative fabrication route was found by investment casting which was quickly developed into a viable alternative. This process allows a much greater design freedom. It is now almost universally accepted to be the best technique for the manufacture of intricate air-cooled high performance gas turbine blades.

1.4.2 Investment casting of polycrystalline turbine blades

To produce an investment casting a wax pattern of the finished article is covered with many layers of a ceramic material until a shell is formed. The wax is then melted out in an autoclave and an induction melted charge is poured into the mould to produce an exquiaxed polycrystalline product. Product quality is improved if the process is performed under vacuum because the loss of the more volatile elements to the air or to metal-crucible interactions is reduced.

Blades cast in this way are known as conventionally cast turbine blades: an example is shown in figure 1.7(a). After casting they are heat treated to optimise γ' and carbide distributions; they are then machined, tested and installed in engines where they operate at temperatures of up to 1100K.

As stated earlier, blades must have high and intermediate temperature creep resistance. When creep occurs in polycrystalline materials the

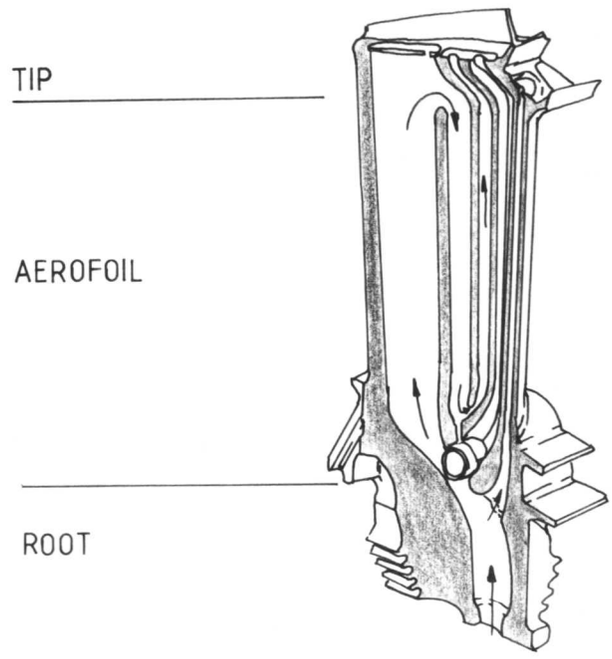

Fig. 1.6. Cut-away diagram of an air-cooled turbine blade showing the complex internal cooling passages.

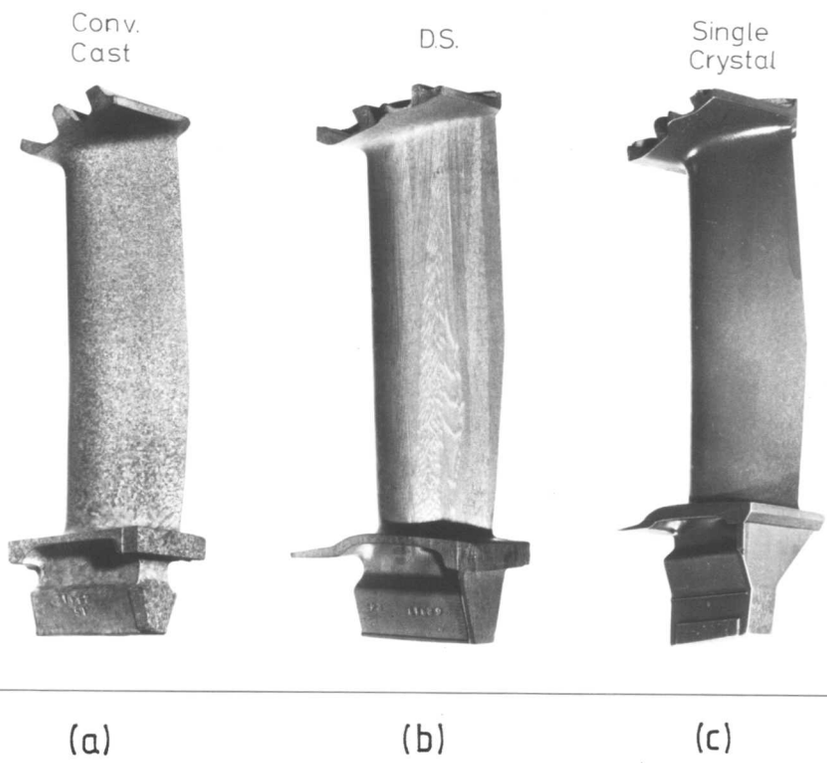

Fig. 1.7. Half scale photograph showing the macrostructures produced by (a) conventional casting, (b) directional solidification, and (c) single crystal casting.

major effects are grain boundary sliding, intergranular cavitation and excessive boundary precipitation. The most serious effects occur along grain boundaries perpendicular to the radial stress direction (eg Ver Snyder and Guard, 1960 and Piearcey and Terkelson, 1967). Figure 1.7(a) shows that the conventionally cast turbine structure contains small equiaxed grains with many high-angle grain boundaries. Sliding within such structures would be severe if it were not controlled by the precipitation of small globular carbides and borides along the grain boundaries.

Given that the most serious cavitation occurs along the grain boundaries perpendicular to the radial stress axis a significant increase in creep resistance can be obtained from a columnar grain structure with boundaries running from the blade root to the blade tip. Structures of this type are referred to as directionally solidified (DS) structures. The principle is to cast the molten charge automatically, under vacuum, into an open ended preheated ceramic shell mould standing on a water-cooled copper chill (fig. 1.8). Chill crystals nucleate and grow up into the head of molten metal. The mould is slowly withdrawn from the furnace to keep the solidification front at the maximum temperature gradient. This results in the growth of large dendritic columnar crystals (figure 1.7b). In DS FCC materials growth is most favourable for grains with <001> directions along the withdrawal axis. Because growth will occur at the same speed on all the close packed planes, in FCC these are {111}, the dendrite tip will be shaped like a pyramid with a <001> vertex (fig. 1.9 and Chalmers, 1954). The blade produced has a <001> orientation along the radial stress axis. The orientation of grains in other directions is not controlled. This orientation is convenient since superalloys have their best thermal fatigue resistance along this direction.

Grain boundaries are still present in the structure and these must be strengthened by the inclusion of small amounts of grain boundary

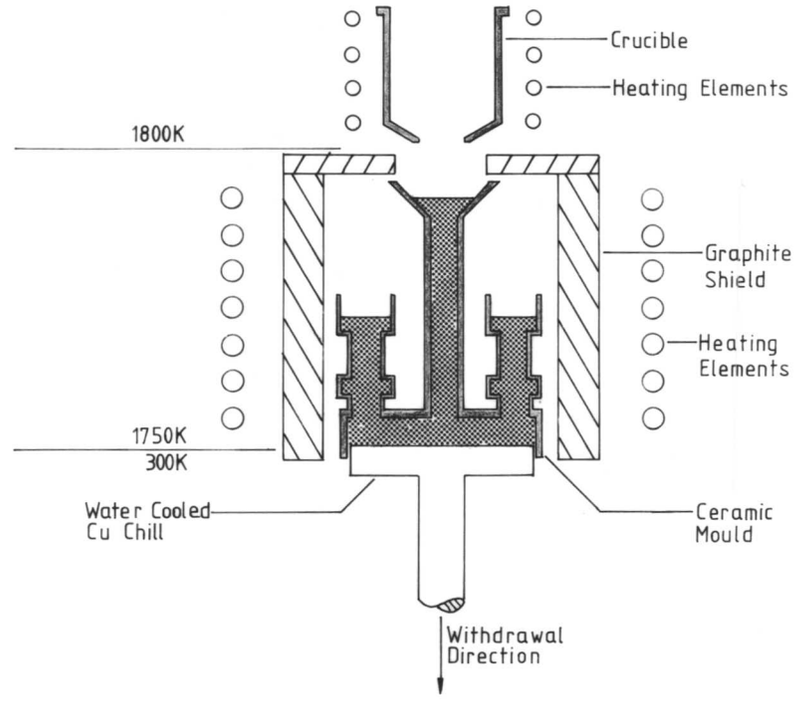

Fig. 1.8. Schematic diagram of a section through a directional solidification furnace.

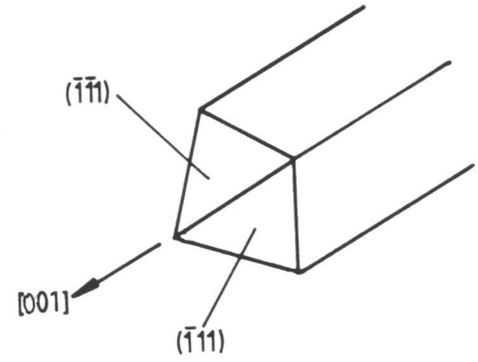

Fig. 1.9. Diagram of a fast growing dendrite tip showing how the four close packed {111} planes produce a dendrite with an [001] vertex.

strengthening elements.

To maintain columnar growth the solidification process is slow. This leads to severe segregation of some elements. This inhomogeneity prevents complete solid solution treatment of the product because small regions melt before the γ' solvus is exceeded. Local melting is known as incipient melting and in most polycrystalline superalloys the incipient melting point is below the γ' solvus. A more detailed discussion of heat treatment is presented in chapter 2.

Despite these heat treatment problems DS blades show a marked increase in ductility, thermal fatigue resistance, stress-rupture properties and intermediate temperature creep properties over their conventionally cast counterparts. Mar-M 002 and Mar-M 200 are two of the best DS superalloys available. After partial solution treatment and careful aging they can be used in gas turbine operation for long periods at temperatures of up to 1300K.

1.4.3 Investment casting of single crystal turbine blades

Most failures of DS blades originate at the grain boundaries so further improvement in properties should be gained by the exclusion of all high angle grain boundaries to form a single crystal product. Industrial 'single crystals' contain a small number of low angle boundaries. They can be grown by a small modification to the DS mould (see for instance Piearcey, 1970 and Ver Snyder and Shank, 1970) to include a helical grain selector between the base of the mould and the blade cavity as shown in figure 1.10(a). Columnar crystals are nucleated on the water cooled copper chill; they grow up into the selector. The helix gradually eliminates grains until only one enters the mould cavity. This is grown out to form the single crystal turbine blade (fig. 1.7c). A component grown in this way has a <001> crystal orientation parallel to the growth direction but the orientation perpendicular to the growth direction is not

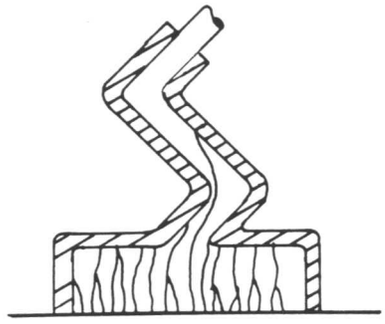

(a)

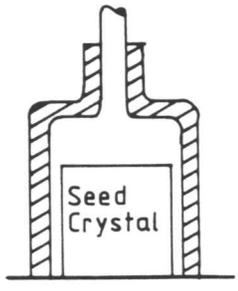

(b)

Fig. 1.10. Single crystal production methods using (a) a helical grain selector and (b) a seed crystal at the base of a ceramic shell mould.

controlled. A precisely positioned seed crystal (fig. 1.10b) can be used in the base of the mould in place of the helix if all the crystal orientations need to be precisely controlled.

Since single crystals contain only a few low angle boundaries they require no grain boundary strengthening additions. This leads to simpler alloy compositions (eg. SRR 99, table 1.1) which produce less severe segregation patterns. The γ' solvus is below the incipient melting point so it is possible to fully heat treat the structure to produce a uniform microstructure of small equiaxed γ' precipitates in a γ matrix (chapter 2).

Commercial data have shown that single crystal turbine blades have microstructural stability up to 1370K and if they are air-cooled they should be able to operate at TETs of up to 1600K. Single crystals improve on DS polycrystals by showing further increases in ductility, thermal fatigue resistance, stress-rupture life and intermediate temperature creep life. Figure 1.11 shows the stress-rupture property advantage of single crystals by comparing creep curves at 1250K and 207MPa for conventionally cast, DS and single crystals made from the same material.

1.5 Strengthening Mechanisms in Ni-base Single Crystal Superalloys

A superalloy single crystal is equivalent to one grain containing a few low-angle boundaries and many γ/γ' interfaces. Methods of alloy strengthening by pinning the boundaries with carbides are totally inapplicable; as a result, the alloys contain no grain boundary strengthening additions and the carbon content is minimised.

The most useful strengthening mechanisms are those which prevent deformation by impeding the movement of dislocations through the material; the two most potent methods being precipitation hardening and solid solution strengthening. In single crystal superalloys most of the strengthening is achieved by the γ' precipitate slowing or stopping the

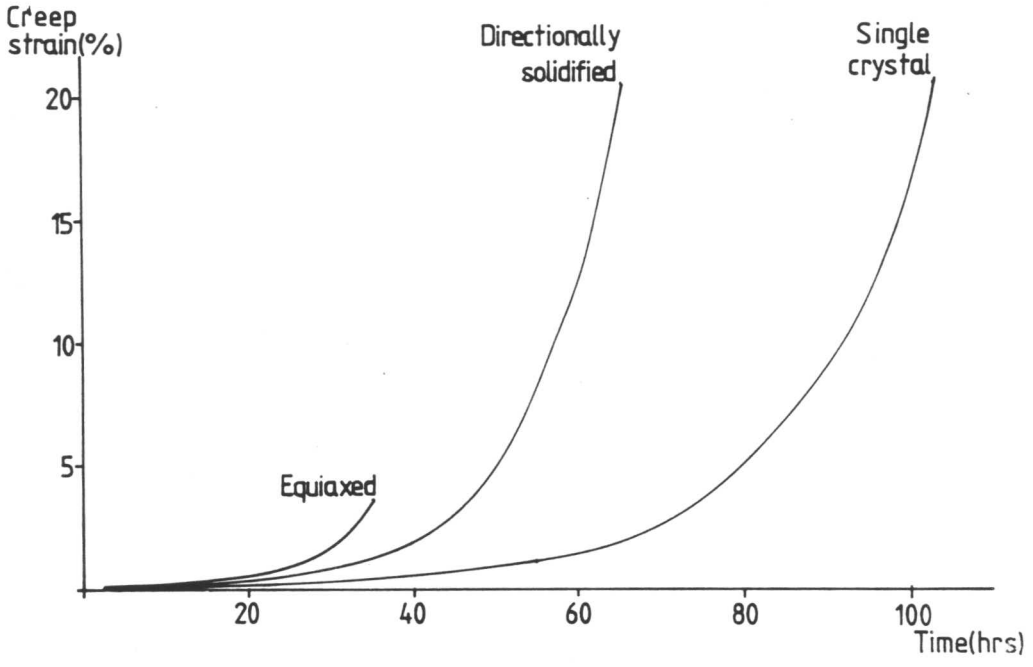

Fig. 1.11. Comparison of the creep strength of conventionally cast, directionally solidified and single crystal superalloys. (Driver et al., 1981.)

passage of dislocations either by forcing them to by-pass or shear through the particles. In addition, solid solution strengthening of the γ matrix reduces the mobility of dislocations between the γ' particles.

1.5.1 Solid solution strengthening

The requirements for solid solution strengthening are the largest possible difference in atomic size and a large range of solid solubility between solute and solvent atoms. Also, to give high temperature strengthening, the solute should have a higher melting point than the solvent and, to give creep resistance, a low diffusivity in the solvent. The γ matrix, which is essentially nickel, adequately fulfils these requirements by having a high solubility for many solute elements, most of which have a low diffusivity in nickel.

At intermediate and high temperatures ($>0.6T_m$) the likely γ deformation mechanisms involve dislocation cross-slip, climb and the diffusional relief of stress. Cross-slip can be reduced by adding elements which lower the γ stacking fault energy to produce wider dislocation dissociations. Volume diffusion rates are generally lowered by alloying with slow diffusing elements. In practice all solid solution strengthening additions are limited by the precipitation of deleterious phases, such as sigma (Decker, 1969).

The major solid solution strengtheners in the alloys under investigation are cobalt, chromium and tungsten. Titanium is also a potent solid solution strengthener but is included mainly to strengthen γ'. These elements were shown to be effective by Pelloux and Grant (1960) who studied the effect of Co, Fe, Cr, Al, Ti and V on the room temperature strength of binary solid solutions with nickel. Some of the strengthening results from the lowering of the stacking fault energy as shown by Beeston and France (1968) and Beeston, Dillamore and Smallman (1968). High temperature strength is due, in part, to the slow diffusing tungsten which

also lowers the diffusivity of Ti and Cr in Ni at 1173K (Pridantsev (1967).

1.5.2 Precipitation hardening

Most of the strength of single crystal superalloys results from the precipitation of the $L1_2$ gamma prime, γ'. The similarity in structure and lattice parameter of γ and γ' allows homogeneous nucleation of coherent, reasonably ductile γ' which has extraordinary high temperature stability. γ' nucleates as coherent spheres, but often adopts a cubic morphology during growth. Havalada (1969a) showed that the shape change was, in part, due to γ/γ' misfit. He also suggested that some other factor had an effect. Figure 1.12 is a TEM micrograph taken of alloy A showing the alignment of γ' cubes along the <001> γ directions.

Like the γ matrix the γ' precipitates can accommodate varying amounts of solute elements. These can substitute on Ni and/or Al sites. Decker (1969) has schematically shown (fig. 1.13) that Co occupies Ni sites, V occupies Al sites and Mo, Cr and Fe occupy either site. Blavette and Bostel (1984) have confirmed Decker's observations using time-of-flight FIM and also shown that Ta and W occupy Al sites.

Misfit strengthening

Misfit strengthening occurs when there is a slight difference between the γ and γ' lattice parameters. The strained region will then retard the passage of dislocations through the interface. Replacement of Al in the γ' by Ti was found to increase the γ/γ' misfit (Decker and Mihalisin, 1969). They also showed that Ti raised the stress-rupture and creep life and decreased the γ' growth and coalescence rate.

Titanium is the element most easily absorbed into the Ni_3Al structure. Taylor and Floyd (1952) and Nordheim and Grant (1954) showed that up to two-thirds of the Al sites could be occupied by Ti; Havalada (1969b) showed that this proportion was increased further when W was present. Titanium is such a beneficial addition to γ' that most commercial superalloys

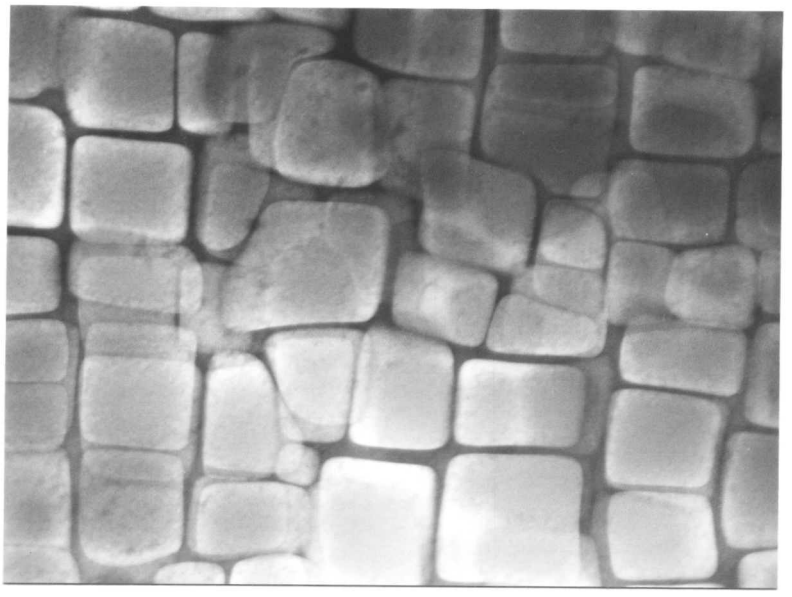

Fig. 1.12. Typical single crystal superalloy microstructure showing γ' cubes aligned in <001> directions. (Foil normal: ~[001].)

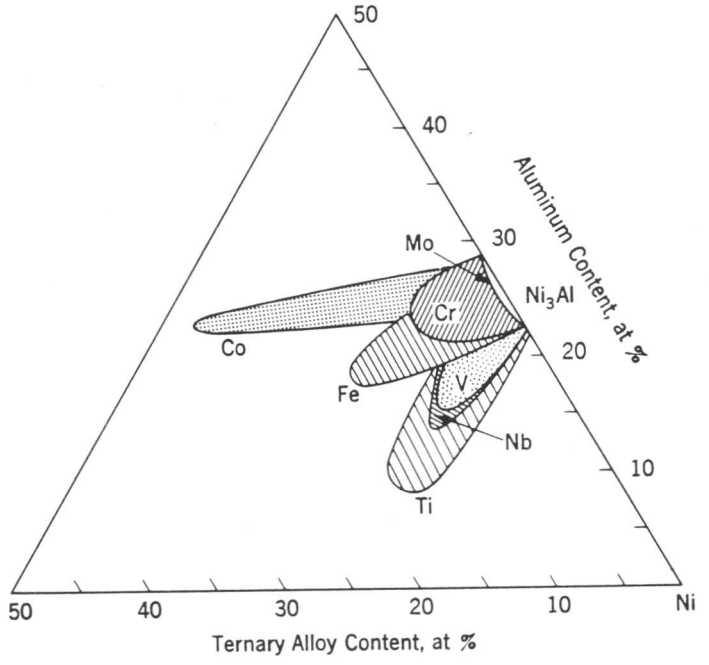

Fig. 1.13. Diagram showing the solid solution fields of various ternary elements in Ni_3Al at 1420K. (Decker, 1969.)

have γ' compositions which are referred to as $Ni_3(Al,Ti)$. In addition to Ti, Nb and Ta also increase the γ' lattice parameters, Cr, Mo and W decrease it, and Co has no effect. Misfit can also be controlled by γ alloying elements; W, Nb and Mo expand the γ lattice parameter, while Co, Cr and Fe have little effect (Decker, 1969).

γ' Particle size

Figure 1.14 shows how the hardness of a Ni, 23at.% Cr, 3.2at.% Ti, 6.4 at.% Al alloy is related to γ' particle size (Mitchell, 1966). The particles are cut by the dislocations on the ascending curve and by-passed on the descending curve. By-passing or Orowan looping (Orowan, 1948) normally only occurs at large particle sizes. Figure 1.14 shows the best properties will be obtained from an alloy which contains the largest particles which will be sheared rather than looped.

γ' Volume fraction

Alloy strength is also increased by increasing the volume fraction of γ'. This is most easily achieved by adding greater amounts of γ' forming elements. Figure 1.15 shows how strength is increased with increasing γ' volume fraction. When alloys contain high volume fractions of small γ' particles deformation occurs mainly by dislocations shearing through the γ', although under certain circumstances looping and climb of dislocations are still important.

Anti-phase boundary and superlattice stacking fault energies

It has been shown (Kear, 1974 and Kear and Oblak, 1974) that as deformation temperature is increased the shearing mode of γ' changes from superdislocation shear, producing anti-phase boundaries (APBs), at low temperatures to partial dislocation shear, producing superlattice stacking faults (SSFs), at intermediate temperatures and finally, back to super-dislocation shear at high temperatures. Different alloys have different

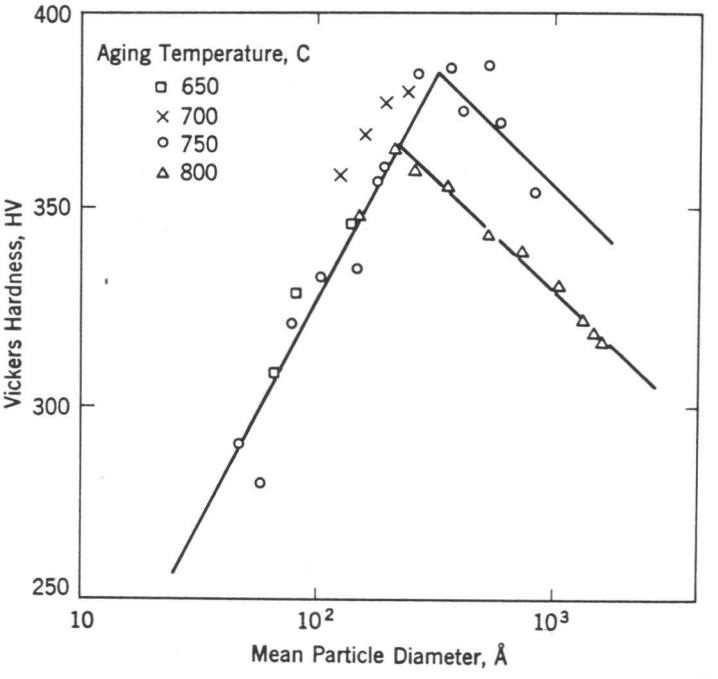

Fig. 1.14. Relationship between particle diameter and hardness for a Cr – Ti– Al alloy. (Mitchell, 1966.)

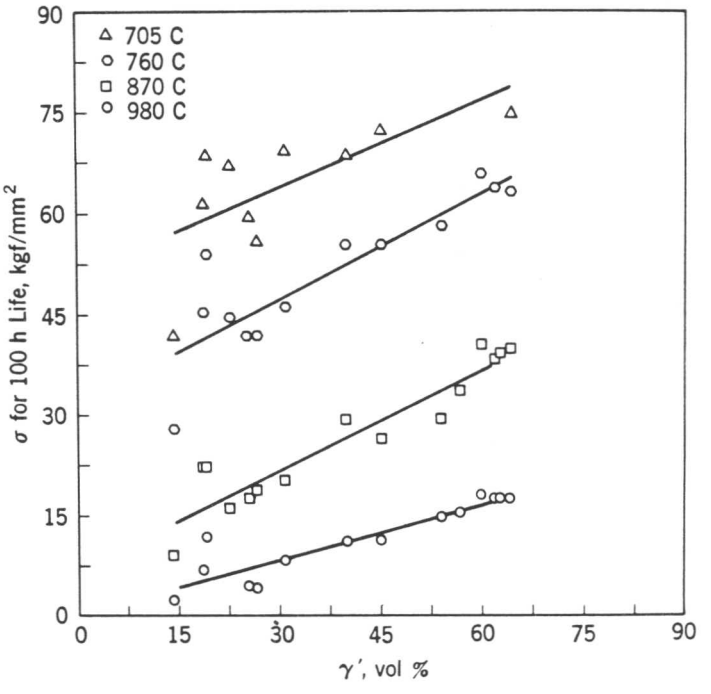

Fig. 1.15. Effect of volume percent γ' on the strength of superalloys at different temperatures.

change-over temperatures but a rough guide is for temperatures up to 1000K to be low temperatures, between 1000K and 1200K to be intermediate and those above 1200K to be high.

Kear et al. (1968) suggested that γ' shearing would take place by the dislocation configuration with the lowest energy. Kear (1974) suggested that the changes in γ' deformation mode may be due to changes in the APB and SSF energies relative to one another (fig. 1.16a). Despite these proposals little effort has been made to establish the APB energy (see 6.2.4) and no effort has been made to evaluate the SSF energies (6.3.4). The effect of γ' composition on the deformation modes of γ' has not been studied prior to this investigation.

The main γ' forming elements in the alloys studied were Al, Ti and Ta. Ti is the major γ' strengthening element and Ta is added to improve high temperature properties by raising the γ' solvus.

1.5.3 Summary

The strengthening mechanisms employed to strengthen single crystal superalloys are:

(i) Solid solution strengthening of γ.

(ii) High volume fraction of γ'.

(iii) γ' particle size.

(iv) Misfit strengthening.

(v) Superlattice stacking fault and anti-phase boundary energies.

Seven alloys (A to G, table 1.2) have been studied. The expected strengthening effect of each of the alloying elements on the Ni base is listed below:

(i) Aluminium
- major γ' forming element.
- γ solid solution strengthener.
- high temperature corrosion resistant Al_2O_3 film effective up to 1530K.

(ii) Cobalt
- γ solid solution strengthener.
- thought to lower the γ stacking fault energy.
- increases γ' stability by reducing the solubility of γ' forming elements in γ.

(iii) Chromium
- γ solid solution strengthener.
- corrosion resistant Cr_2O_3 film, effective up to 1370K.

(iv) Tantalum
- γ' strengthening element giving high temperature stability because of its high melting point.

(v) Titanium
- major γ' strengthening element.
- controls γ/γ' misfit.
- small changes in concentration are thought to have a considerable effect on alloy strength due to changes in the deformation mechanism.

(vi) Tungsten
- γ solid solution strengthener because of its low diffusivity and high melting point.

1.6 The Aim of this Investigation

In their recent review of high γ' volume fraction Ni-base superalloys Pope and Ezz (1984) concluded that although the deformation mechanisms are well understood and the tensile properties are well documented there has been little work on the creep of superalloys or on the creation of a model which links deformation mechanisms to properties. One of the most serious gaps is the lack in understanding of the effects of composition on the flow and creep properties of both single phase γ' and two-phase γ/γ' alloys.

The aim of the present work is to study the influence of titanium content on the defect energies and dislocation structures in a series of single crystal superalloys (table 1.2). No attempt has been made to verify the deformation mechanisms established by others. Attention has been focused on the influence of Ti on the APB and SSF energies of the alloys with a view to relating these parameters via the observed deformation mechanisms, to the performance of the alloys in stress-rupture tests.

It seems (Roome, 1982) that changes of the order of 0.8 at.% in the Ti content have a significant effect on the stress-rupture life of semi-homogenised superalloys. To further verify this effect tests designed by the author have recently been performed on three fully homogenised alloys

(A, D and G of table 1.2). The specimens used for these tests were carefully prepared so factors (i) to (iv) of 1.5.3 were constant. Any changes in behaviour must then be related to factor (v). The results are presented in figure 1.17 and appendix A. It is clear that the stress-rupture life is improved by small increases in the Ti content.

Roome suggested that in addition to the change in mechanism with temperature (fig. 1.16a and Kear, 1974) there was a change in APB energy with alloy titanium content, which may influence the temperature at which the change in deformation mechanism occurs; at higher titanium levels the change occurred at lower temperatures (fig. 1.16b). It was found that longer stress-rupture lives were obtained from higher Ti alloys when γ' shear was occurring by partial dislocations producing superlattice stacking faults.

Kear (1974) and Roome (1982) could not establish their ideas as no accurate values for APB energy and no values for SSF energy as a function of Ti content were available for any superalloy material.

The following chapters describe experiments performed to measure the fault energies in a series of single crystal superalloys which contain systematic variations in Ti content and then discusses the implications of these values to the creep deformation of superalloys.

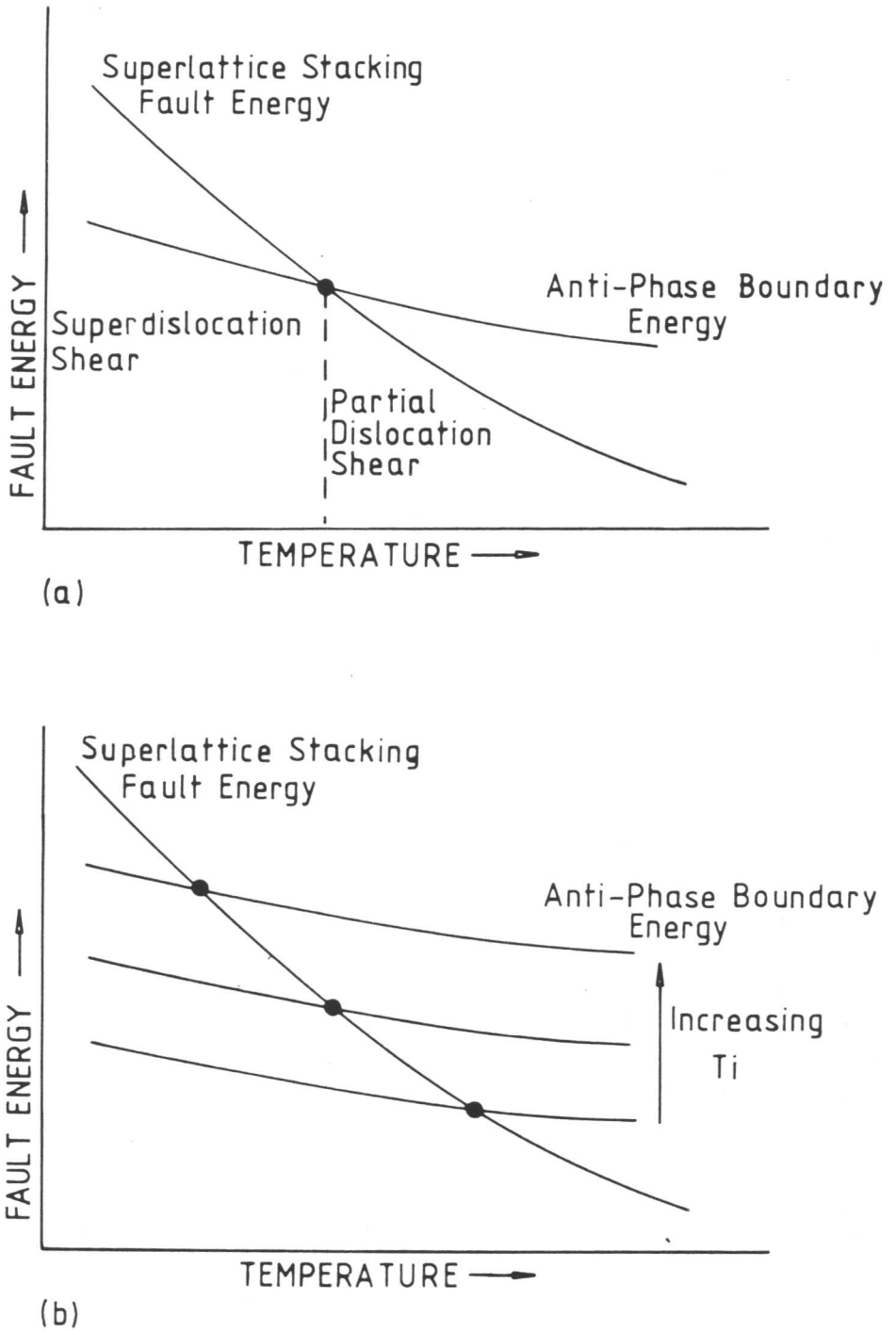

Fig. 1.16. Schematic diagram showing the relationship between deformation mechanism and fault energy (a), and the effect of titanium on fault energy and deformation mechanism proposed by Roome (1974) (b).

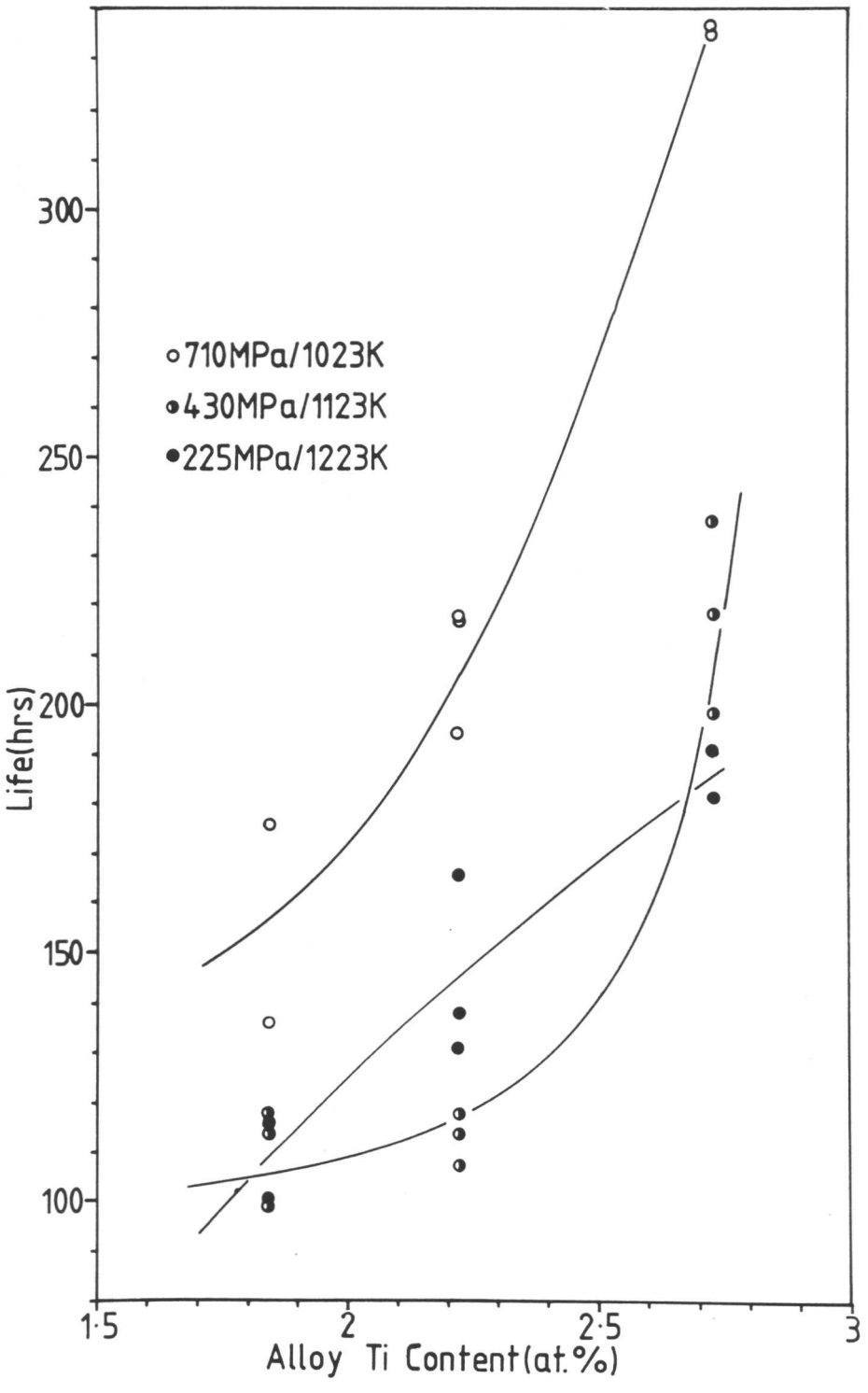

Fig. 1.17. Relationship between stress-rupture life, titanium content and test conditions for alloys A, D and G (table 1.2).

CHAPTER 2

THE HOMOGENISATION BEHAVIOUR OF SINGLE CRYSTAL SUPERALLOYS

2.1 Alloy Supply and As-cast Composition

The compositions of the as-cast alloys used in this investigation are listed in table 1.2. These bulk analyses were gained from X-ray fluorescence performed by Ross and Catherall Ltd., Sheffield. All the alloys were cast as 10mm diameter single crystal rods by Rolls-Royce Ltd., Derby using the technique described in 1.4.3. The small compositional variations were achieved by adding a highly alloyed 'button' of material to a master melt before casting.

2.2 Heat Treatment

As-cast, directionally solidified, single crystal rods of Ni-based superalloys are heavily cored due to non-equilibrium cooling caused by the slow withdrawal from the furnace. During solidification the γ' forming elements are partitioned to the liquid. The enriched interdendritic liquid ultimately solidifies by eutectic decomposition to form a coarse γ/γ' mixture (fig. 2.1b). The as-cast microstructure (fig. 2.1a) contains a fine dispersion of γ' particles in the initially γ dendrites; the coarse γ/γ' eutectic is visible in the interdendritic spaces. The severe coring causes the γ' morphology at the centre of the dendrites (fig. 2.1d) to be considerably different from that at the edge (fig. 2.1c). A small number of carbides are also visible (fig. 2.1e). These precipitate ahead of the alloy solidification front and are essentially unchanged by subsequent heat treatment.

The aim of heat treatment is to remove the inhomogeneity by taking the precipitates into FCC solid solution at high temperature, holding the

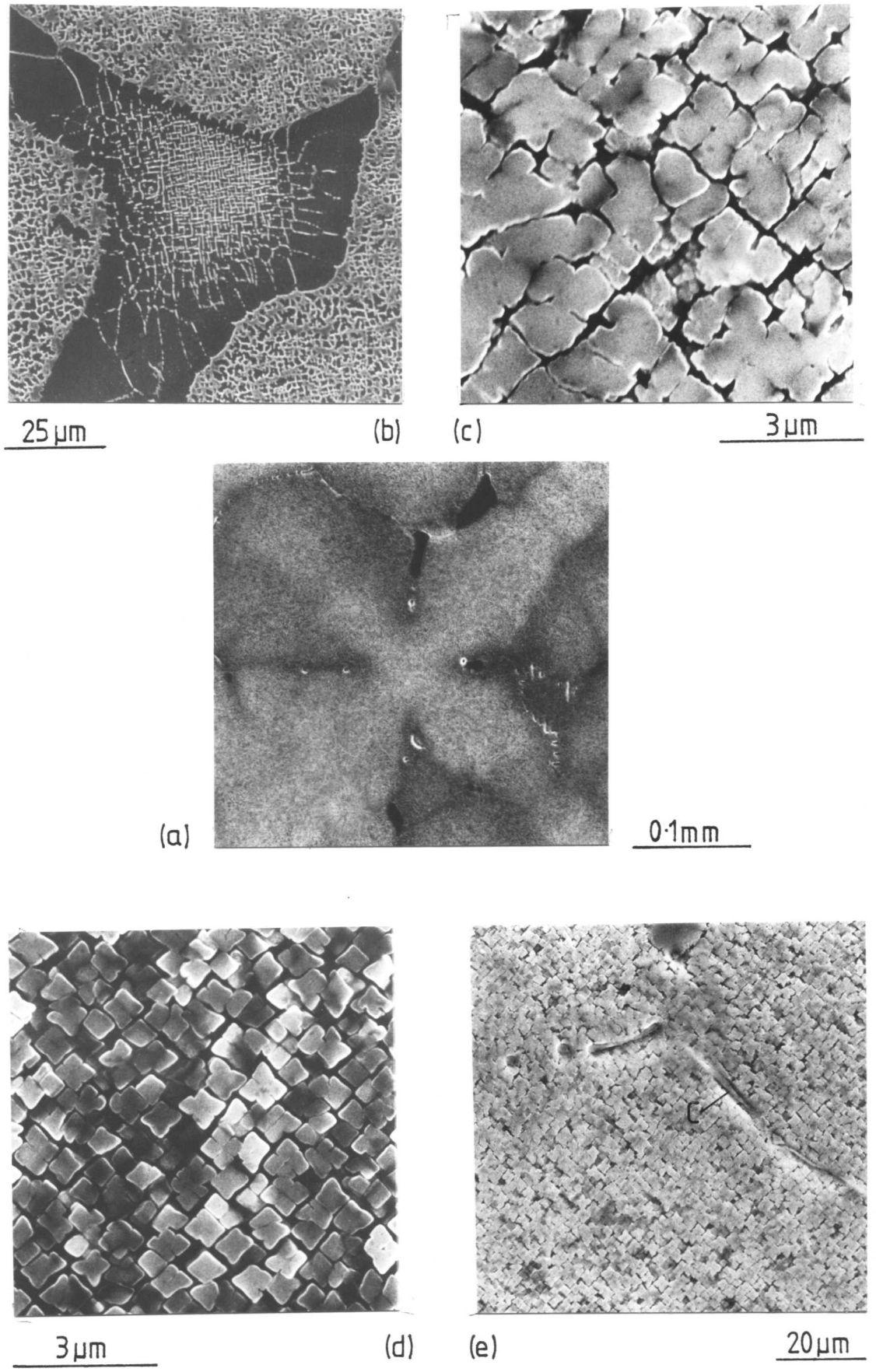

Fig. 2.1. The as-cast microstructure showing: the overall structure (a), γ/γ' eutectic (b), ragged coarse γ' at the dendrite edges (c), regular fine γ' at the centre of the dendrites (d), and dendritic carbide (e). (Etch: electrolytic 10% phosphoric in water for (a), (c), (d) and (e); electrolytic 5% H.F., 10% glycerol and water for (b).)

material at this temperature until all the compositional waves have decayed and then rapidly cooling to precipitate fine, even γ'. Unfortunately in most commercial polycrystalline alloys the inclusion of grain boundary strengthening elements causes the γ' solvus to be higher than the incipient melting point. In these cases 'solution treatment' is undertaken at a temperature as near as possible to the incipient melting point. It is not possible to dissolve the γ' or the γ/γ' eutectic completely so these components, although much reduced, are still present in the treated microstructure. Cooling from the 'solution' temperature precipitates fine γ' between the large γ' particles to produce a dual γ' size distribution. A long aging treatment (normally 16 hrs. at 1140K) is then used to improve γ' shape and to precipitate grain boundary carbides.

Single crystal materials have much higher incipient melting points than conventional alloys; it is possible to solution treat these alloys above the γ' solvus, but below the incipient melting point. This temperature interval is known as the heat treatment window. It is typically 20K wide. At the heat treatment temperature the γ' and the γ/γ' eutectic are completely solutioned enabling complete homogenisation. Reprecipitation of γ' can be controlled to produce a morphologically and chemically homogeneous microstructure of fine equisized γ' in a γ matrix without γ/γ' eutectic.

2.3 Determination of the Heat Treatment Window

An initial attempt to determine the heat treatment window was made using the Stanton-Redcroft DTA673-4 differential thermal analysis system at Rolls-Royce Ltd. Owing to the gradual changes in heat output at the γ' solvus, γ/γ' eutectic solvus and incipient melting point it was difficult to determine accurate temperatures from the DTA traces (fig. 2.2). The errors were assessed to be of the order of ±10K. In many cases the heat treatment window was of that order so a more accurate technique was required.

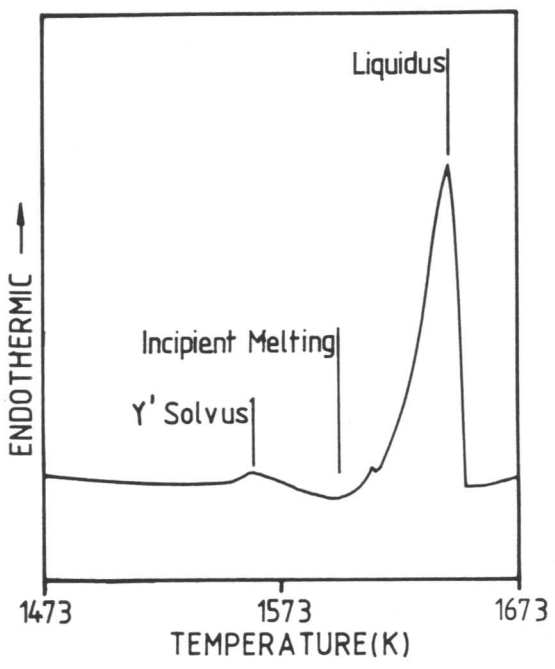

Fig. 2.2. Semi-schematic representation of a typical DTA trace gained from alloys A to G showing gradual changes in heat output.

A simple technique employing optical microscopy was chosen. 15 mm x 10 mm diameter cylinders were heated to temperatures at 10K intervals between 1550 and 1610K for one hour periods then rapidly air cooled to ambient temperature. Incipient melting locally alters the microstructure and was detected on polished and electrolytically etched samples, eg. figure 2.3(b). The temperature at which the γ/γ' eutectic entered solution was similarly determined, eg. figure 2.3(a). It is noted that this is the standard method used to determine the heat treatment windows of commercial alloys. The error in the method was of the order of ±6K.

The results are presented in figure 2.4 which shows that the incipient melting point decreased with increasing titanium content; the eutectic solvus rose and the overall effect was to narrow the heat treatment window with increasing titanium.

The effect of increasing the Ti content is to increase the volume fraction of liquid which decomposes to the γ/γ' eutectic; higher Ti levels thus lead to higher eutectic volume fractions in the as-cast alloy (0.02 in alloy A and 0.003 in alloy G). This means that for a given homogenisation temperature, high titanium alloys will require longer times for the dissolution of the eutectic. Because the heat treatment window assessment procedures were isochronal, high titanium alloys were expected to show an apparent increase in the γ/γ' solvus temperature (fig. 2.4).

In the absence of detailed phase diagram data the effect of Ti on the incipient melting point cannot be properly discussed but the observed effect is consistent with that of titanium (at levels less than 15 at.%) on the solidus temperature of Ni-Ti-Al alloys (Nash, Vejus and Laing, 1982).

2.4 Microanalysis of the As-cast Structure

Microanalysis was carried out on a Cambridge Instruments Microscan 5 electron microprobe (spot size 2μm) and an ISI 100-A SEM with a Link 860 EDS unit (spot size 1μm). The results obtained from both

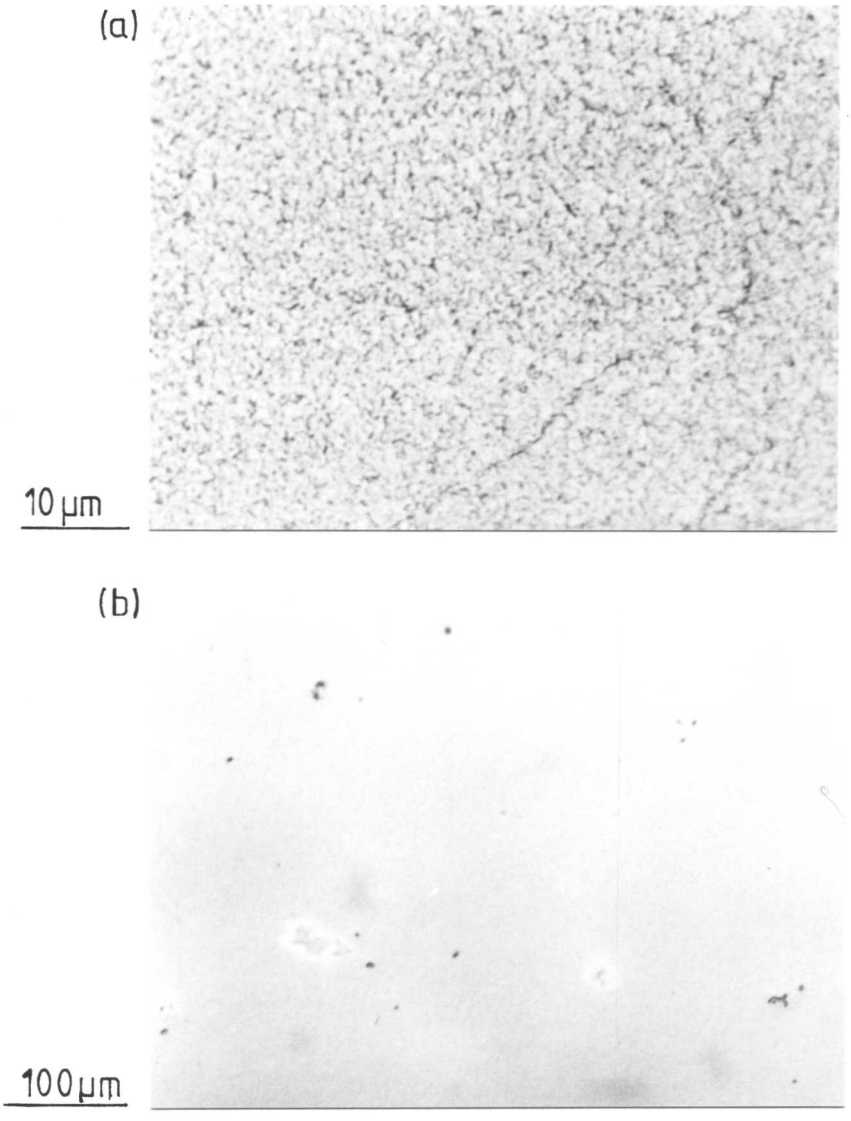

Fig. 2.3. Micrographs of the microstructures at the γ/γ' eutectic solvus (a) and the incipient melting point (b).

Etch: Electrolytic 10% Phosphoric acid in H_2O

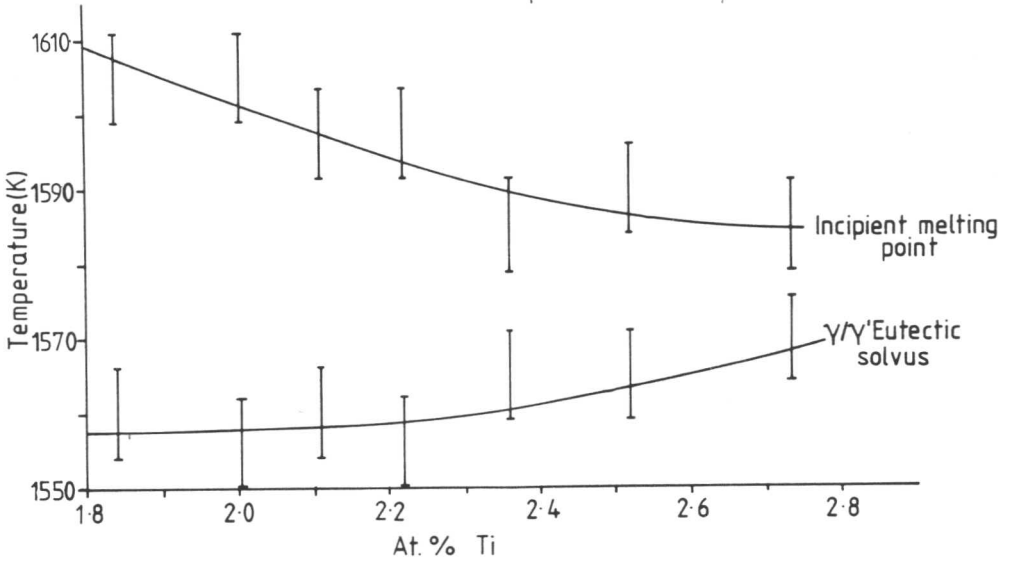

Fig. 2.4. Temperature dependence of the incipient melting point and the γ/γ´ eutectic solvus on the bulk alloy titanium content.

techniques were corrected for atomic number, absorption and fluorescence.

Probe and EDS traces across dendrite arms show relatively high concentrations of Al and Ti, both strong γ' forming elements, at the edges of the dendrites, while W showed high concentrations in the central regions (fig. 2.5). Quantitative metallography on a Quantimet 720 image analysing computer showed that the γ' volume fraction at the edges of the dendrites was higher than at the centres. Alloy A (2.7 at.% Ti) contained 0.6±0.05 γ' at the edges of the dendrites and 0.55±0.05 at the centres; the corresponding results for alloy G (1.8 at.% Ti) showed 0.71±0.05 at the edge and 0.49±0.05 in the centres - see figure 2.1(c) and (d). As expected this indicates that the γ' forming elements are rejected from the solidifying alloy. The difference in γ' morphology between dendrite edges and centres may be due to soft impingement between the rapidly growing γ' particles.

Analysis of the eutectic colonies shows them to be rich in the expelled titanium and aluminium, and deficient in chromium and tungsten (fig. 2.6). Quantitative microscopy showed that the eutectic in alloy A contained 0.93 γ' and 0.17 γ. Figure 2.6 indicates that there are large concentrations of Cr and Ti near the eutectic interfaces. This segregation pattern is similar to that observed by Piearcey, Kear and Smashey (1967). However, the cause of this extreme segregation is unclear. If the solidifying eutectic were expelling non-γ' forming elements then such strong titanium segregation is unlikely. An explanation could be that the analysis spot has passed over a small Ti rich carbide although none is visible in figure 2.6.

2.5 Homogenisation

A temperature of 1573K was chosen for this experiment since it lies within the heat treatment window of all the alloys. Homogenisation was carried out on samples of alloy A sealed in a silica tube containing a

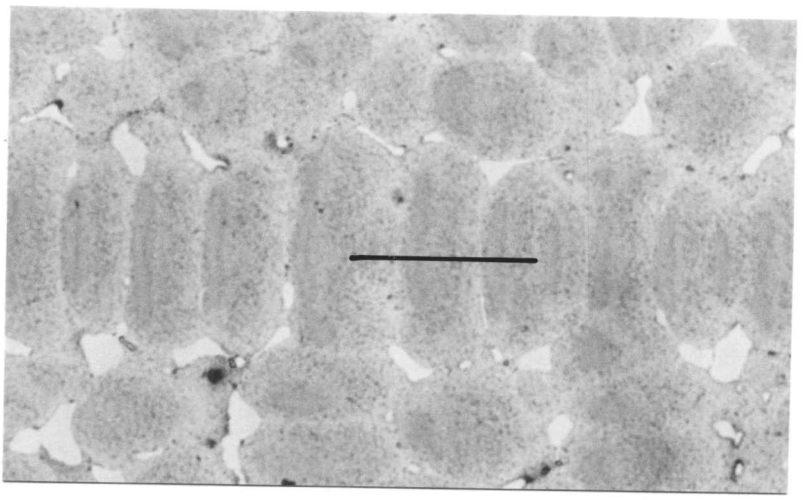

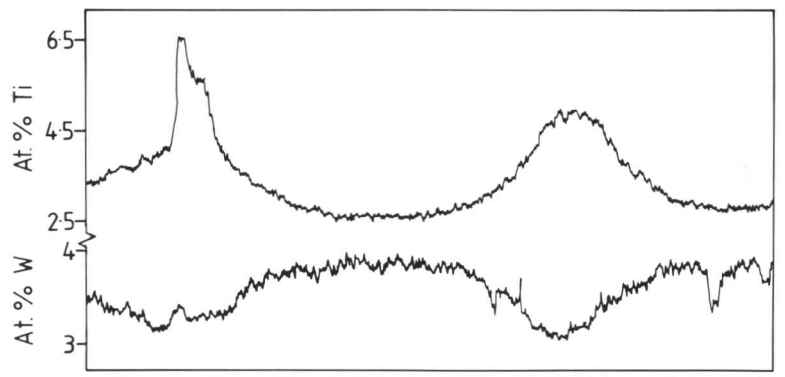

Fig. 2.5. Electron microprobe traces for Ti and W (b) across two secondary dendrites arms shown in (a).

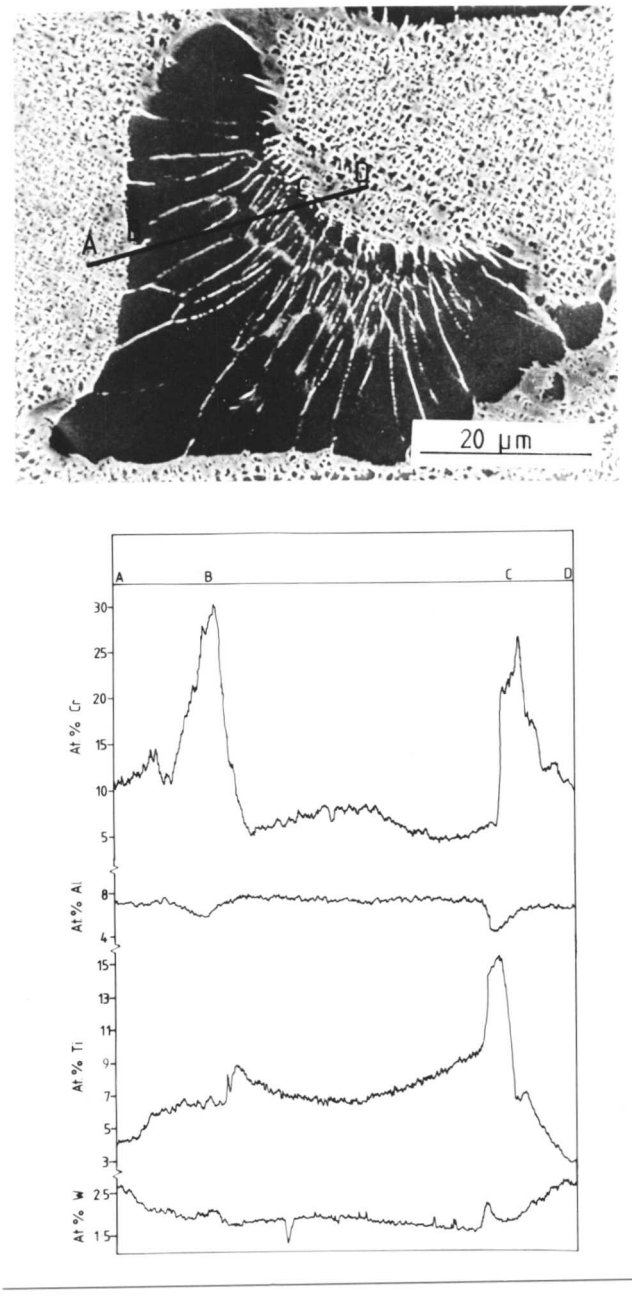

Fig. 2.6. Electron microprobe traces for Cr, Al, Ti and W across a typical γ/γ' eutectic colony.

partial pressure of Ar. The experiment was interrupted after 4, 8, 16, 32 and 64 hours at temperature for examination. A fiducial line marked on the specimen was used; after each heat treatment SEM/EDS analyses were made on this line at 10μm intervals. This experiment was only designed to show overall macroscopic composition variations.

Heat treatment for 8 hours at 1573K produced an apparently uniform microstructure, figure 2.7(a), but analysis showed that the compositional variations were still present. After 16 hours the Ti, Ni, Al and Cr concentrations showed no significant variations while after 32 hours none of the elements exhibited segregation beyond the range of the experimental error.

An attempt was made to assess the segregation profiles in terms of a relaxation time, t, where:

$$t = \frac{d^2}{D} \qquad \text{eqn. 2.1}$$

The system was simplified to a solid solution of the most severely segregated element, W, in Ni at 1573K. It was found, appendix B, that the calculated relaxation time was similar to that determined experimentally. It appears that the homogenisation time of the whole alloy can be approximated to the homogenisation time for a binary solid solution of the most severely segregated element with Ni. It is suggested that further work be undertaken on different alloys with different amounts of segregation to show if this simple method can be used to predict the time necessary to achieve adequate homogenisation of complex superalloys without the need for much time-consuming experimentation.

2.6 Homogenised Microstructure

2.6.1 Growth of the γ' precipitate

For convenience, a homogenisation time of 36 hours at 1570K was used. The specimens were air cooled; the microstructure shown in figure 2.7(b) was produced. To facilitate easier measurement of the

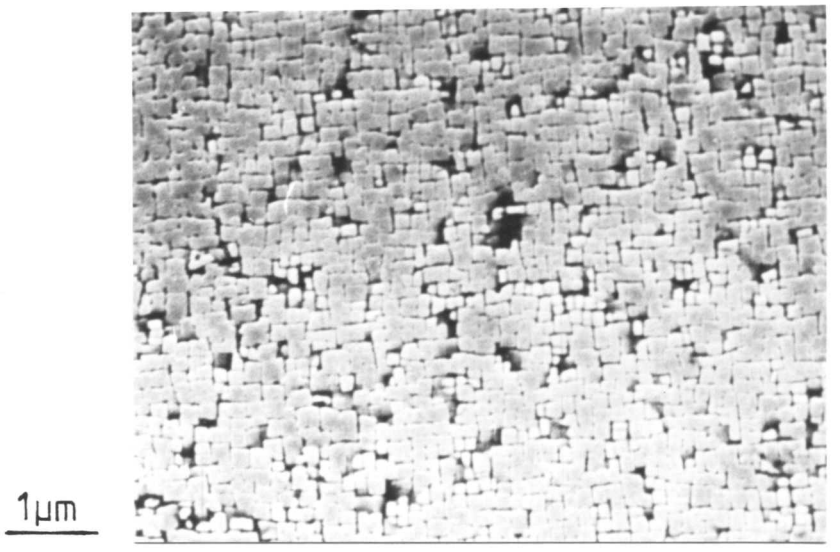

(a)

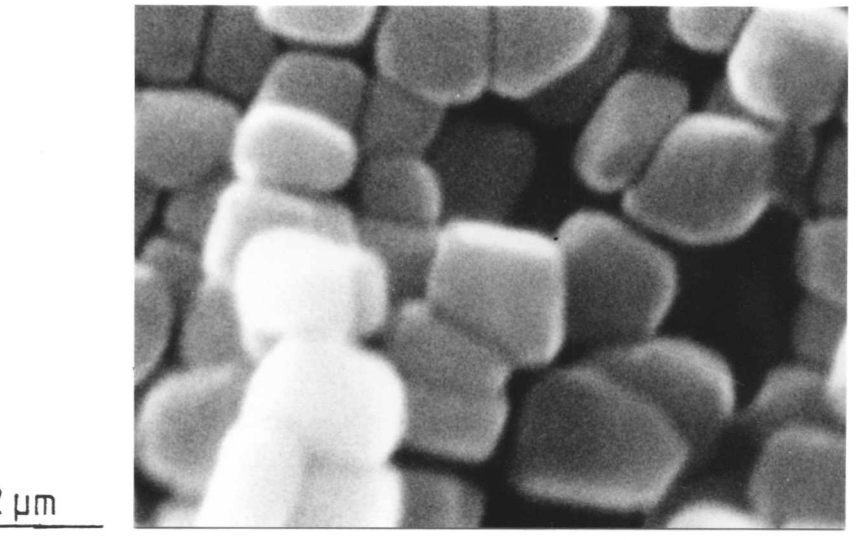

(b)

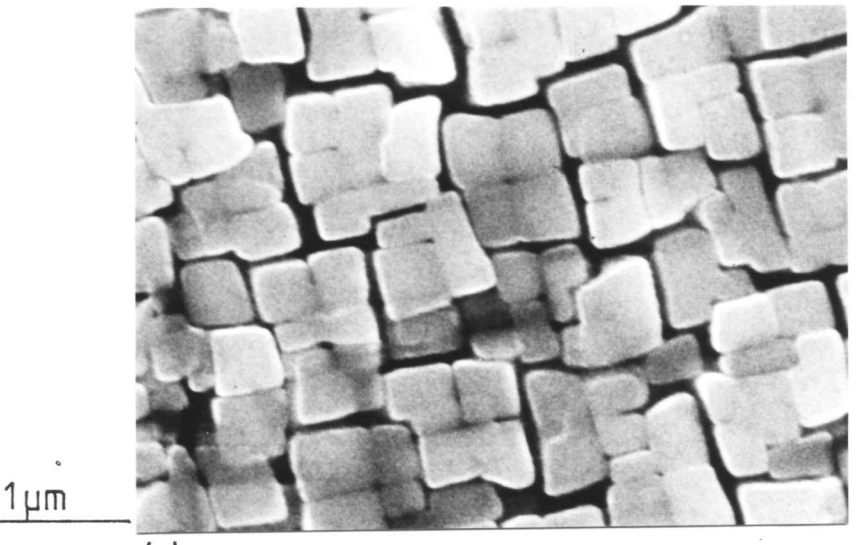

(c)

Fig. 2.7. Micrographs showing the microstructures produced after homogenisation for 8 hrs at 1570K (a) and 32 hrs at 1570K (b), and 36 hrs at 1570K followed by 16 hrs at 1390K (c).

superlattice defect energies it was decided to increase the γ' size from about 0.2μm to about 0.5μm. Facilities were available for this to be done either by slow cooling from the homogenisation temperature or by a further heat treatment at a temperature just below the γ' solvus. Both methods were tried. Slow cooling at 30K/min. produced an unsatisfactory microstructure containing an irregular γ' size distribution. By heat treating for 16 hours at 1390K a suitable microstructure consisting of an even distribution of similar sized γ' octdoadigally diced cubes (fig. 2.7c). The growth of gamma prime to form octdoadigally diced cubes proceeds by the development of solid state dendrites, with {001} facets, in <111> directions, figure 2.8, as discussed by Ricks, Porter and Ecob (1983). In most high γ' volume fraction alloys soft impingement prevents the growth process passing stage (e) of figure 2.8. This can be clearly seen in the final heat treated microstructure shown in figure 2.7(c).

2.6.2 Microanalysis of the homogenised structure

Fine scale compositional variations within the homogenised microstructure were studied using a Philips 400T TEM/STEM with a Link 860 analysis unit. Thin foils were manufactured by the route described in 3.3.1. Foil thicknesses were determined using the convergent beam method described by Kelly, Jostsons, Blake and Napier (1975). At least ten γ' areas and six γ areas were analysed in each of the seven alloys. The spot size used was 20nm (after allowing for beam broadening in the foil) and the results were corrected for atomic number and absorption; typical analysis points are shown in figure 2.9.

Analysis of the dendritic carbide showed it contained 42 at.% Ti, 31.5 at.% Ta, 19 at.% W and 8 at.% Ni. There was little compositional or morphological change between the as-cast and heat treated carbides.

The γ and γ' analyses collected are listed in tables 2.1 and 2.2. It is worth noting that for most elements the errors in the γ analysis were

Table 2.1. Gamma Prime Compositions (at.%)

	Alloy							
Element	A	B	C	D	E	F	G	Error
Ni	67.8	72.4	71.3	70.5	70.6	71.0	69.8	±0.7
Al	18.6	13.8	15.9	17.1	16.6	17.0	17.2	±0.8
Ti	3.9	3.8	3.5	3.3	3.2	3.1	2.8	±0.2
Cr	3.9	3.8	3.3	3.5	3.3	3.4	4.0	±0.2
Co	3.1	3.1	2.9	3.0	2.9	2.6	3.0	±0.2
Ta	1.2	1.3	1.2	1.3	1.5	1.2	1.2	±0.1
W	1.4	1.2	1.9	1.4	1.9	1.6	2.0	±0.2

Determined by EDS of 10 sample points per alloy

Table 2.2. Gamma Compositions (at.%)

	Alloy							
Element	A	B	C	D	E	F	G	Error
Ni	63.0	65.2	64.9	66.1	63.9	64.0	64.1	±1.3
Al	9.7	6.1	11.1	9.1	8.5	8.7	8.7	±0.9
Ti	1.7	1.2	1.5	1.5	1.1	0.9	0.9	±0.2
Cr	17.1	17.6	14.7	14.6	18.2	17.0	17.0	±1.5
Co	6.3	7.0	5.9	6.2	6.5	6.6	6.6	±0.4
Ta	-	0.1	0.1	0.3	0.4	0.3	0.3	±0.3
W	2.3	2.4	2.9	2.2	2.4	2.5	2.5	±0.2

Determined by EDS of 6 sample points per alloy

Errors quoted are the standard deviations for each of the alloys.

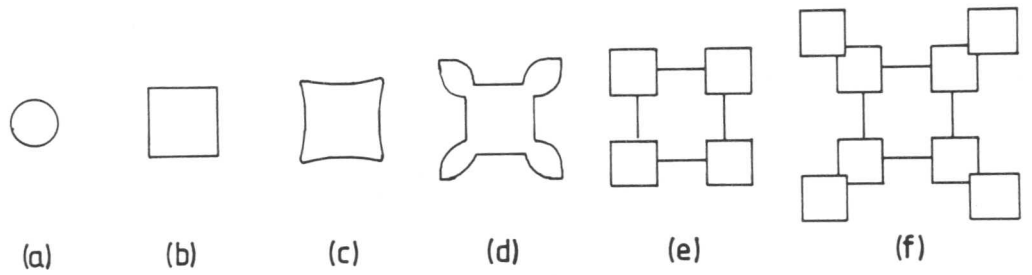

Fig. 2.8. Diagram showing the stages in the growth of a γ' precipitate (after Ricks et al., 1983).

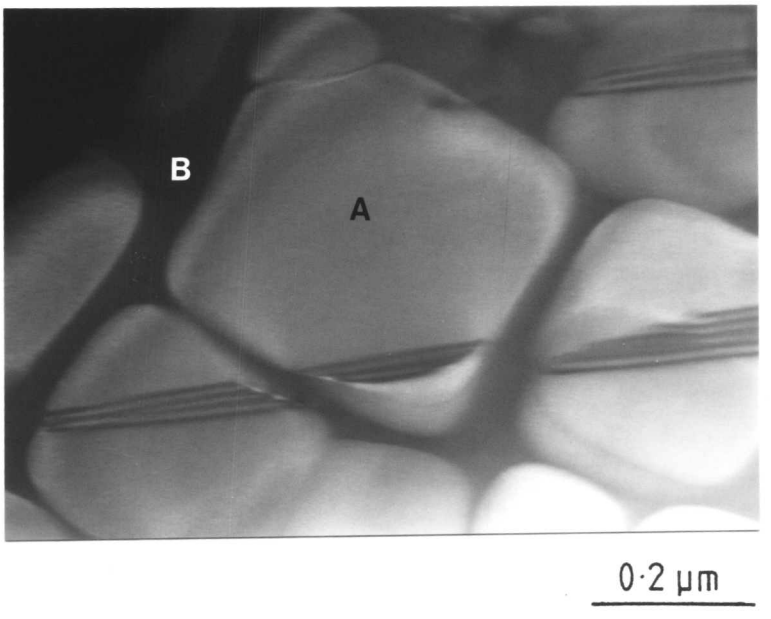

Fig. 2.9. Bright field transmission electron micrograph showing typical γ' (A) and γ (B) analysis points used to obtain the compositions reported in tables 2.1, 2.2 and 2.3.

significantly larger than those in the γ' regions. This was because in these alloys the γ regions were so narrow that the broadened beam almost certainly passed through a small amount of the γ'. The aluminium analyses were not thought to be accurate due to the way in which the Link 860 software performs the background subtraction - appendix C.

Tables 2.1 and 2.2 show that the heat treatment was sufficient to give an acceptably homogeneous product. As shown, the error in the Ti determination was assessed to be ±0.2 at.%. Table 2.3 shows that the interval in Ti content between the alloys was less than the error in their determination. Consequently it was decided to study three significantly different alloys. The alloys chosen were A, D and G; table 1.2 shows that these alloys were identical except for the systematic replacement of some Ni by Ti.

The results in tables 2.1 and 2.2 show that Al, Ti and Ta partitioned to the γ' phase and that Co, Cr and W partitioned to the γ. Table 2.3 shows that as the alloy Ti content was increased, the level in the γ' gradually rose as did the level in the γ.

It must be noted that these microanalysis results were obtained from the Link 860 with no additional corrections. They must therefore be treated as comparisons of one alloy with another and not as absolute accurate analysis values.

2.7 Lattice Parameter and Alloy Misfit

The γ' lattice parameter of alloys A, D and G was obtained by X-ray powder photography in a Debye-Scherer camera using CuK_α radiation. Extracts of γ' were obtained from homogenised alloys electrolytically using a solution of 20% phosphoric acid in water containing 4 gm/l of tartaric acid, to suppress the formation of heavy metal hydroxides, at room temperature. This is the technique used by Rolls-Royce Ltd. TEM examination of a sample of the extract showed no evidence of residual γ on the γ'. Extracts of γ were

Table 2.3. Alloy, γ and γ' Ti Contents (at.%)

Alloy	A	B	C	D	E	F	G
Bulk composition	2.7	2.5	2.4	2.2	2.1	2.1	1.8
γ' composition	3.9	3.8	3.5	3.3	3.2	3.1	2.8
γ composition	1.7	1.2	1.5	1.5	1.1	0.9	0.9

error = ±0.2

Table 2.4. Lattice Parameters of Alloys A, D and G from X-ray Powder Diffraction Photographs (Kenyon, 1983)

Alloy	Overall Ti content (at.%)	γ' Ti content (at.%)	γ Ti content (at.%)	Corrected lattice parameter, a (nm)	
				γ'	γ
A	2.7	3.9	1.7	0.35823	0.35810
D	2.2	3.3	1.5	0.35808	-
G	1.8	2.8	0.9	0.35797	0.35800

error in a = ±0.00005nm

also manufactured by an electrolytic method in 5% hydrofluoric acid, 10% glycerol and 85% water at room temperature. A stainless steel cathode was used; unfortunately this reacted with the electrolyte to produce an unidentified iron compound. The addition of tartaric acid suppressed this reaction sufficiently for γ lattice parameter determinations to be made for alloys A and G. It was not possible to see if any γ' was present in the extract by TEM (Kenyon, 1983).

Powder films were taken using an exposure time of 2 hours and the lattice spacings and unit cell size were calculated by the normal methods (Cullity, 1978).

In table 2.4 it is shown that as the Ti content increases so the γ' lattice parameter increases. This disagrees with Nordheim and Grant (1954) who have reported that the lattice parameter of Ni_3Al changed by only 1% when 60 at.% Ti was added. However, the results of Fell (1961) agree with the observations made in this investigation: no change in misfit was predicted as table 2.3 shows that the γ Ti content rises in unison with the γ' Ti content.

The misfit values calculated using the formula:

$$M = \frac{a_{\gamma'} - a_{\gamma}}{a_{\gamma'}} \qquad \text{eqn. 2.2}$$

were smaller than the errors. It was concluded that there was no measurable γ/γ' misfit. The fact that the γ' particles observed in the alloy were cubic even though low misfit alloys are expected to contain spherical particles supports the suggestion, previously reported, of Havalada (1969a) that precipitate shape is affected by factors other than the γ/γ' misfit. It is thought that soft impingement between the growing γ' particles could explain this observation.

The <u>in situ</u> misfit was measured using the convergent beam HOLZ method of Ecob, Ricks and Porter (1981). As expected, no misfit was detected; any misfit would be taken up by the γ' planes pulling the planes

of the narrow γ regions to match the lattice parameters.

Although no γ/γ' misfit could be detected at room temperature, it may be that there is a difference in thermal expansivity between γ and γ' which will result in a misfit at higher temperatures. No data are available for the thermal expansivity of γ and γ' and no measurements of misfit have been undertaken at high temperatures. These experiments could provide some useful information about deformation of superalloys at high temperatures.

2.8 γ' Long Range Order Parameter

The APB energy of a material is closely related to its degree of ordering. As one of the aims of this project is to evaluate the APB energy it would perhaps be useful to relate the energy values to the degree of ordering. Mihalisin (1969) found that the order parameters of γ' extracted from IN-731, 713C and 713LC were high (~0.95) in IN-713C and LC, and that they were largely unchanged by heat treatment.

Calculation of the order parameter involves comparing the relative intensities of a fundamental line and a superlattice line. (100) is usually chosen as the superlattice line and (200) as the fundamental. These are high intensity lines which eliminate any preferential orientation effects. Diffractometer traces and Guinier camera films of the alloys studied showed no superlattice lines with an intensity significantly above the background value, thus making it impossible to calculate the order parameter.

Reference to table 1.2 shows that these alloys contain significant amounts of W and Ta; elements which strongly absorb X-rays. It is possible that the presence of these elements reduces the intensity of the superlattice lines to undetectable levels. The effect has previously been observed by Oblak and Kear (1972) in Mar-M 200.

It has been assumed that the order parameter is greater than 0.8, the lowest value reported by Mihalisin, and at room temperature there

was no significant change in ordering through the alloy series. It would be interesting to perform a heating experiment on a γ' extract to see if order parameters can be calculated at higher temperatures.

2.9 Conclusions

(i) The results indicate that Ti decreases the width of the heat treatment window for cast single crystal superalloys due not only to the lowering of the solidus with increasing Ti, but also because the volume fraction of γ/γ' eutectic increases with overall Ti concentration. The effect could be mitigated by means of longer heat treatments which would have the effect of reducing the apparent γ/γ' eutectic solvus.

(ii) The alloys achieve adequate homogeneity after annealing at 1570K for 32 hours (36 hours was used for reasons of convenience) and this homogeneity is both long range and on the level of individual γ' particles.

(iii) Subsequent heat treatment at 1390K for 16 hours grows the γ' from 0.2μm to 0.5μm without any observable loss in coherency or change in composition.

(iv) Increasing the Ti content increases the γ' and γ lattice parameters but not the γ/γ' misfit.

(v) The measured misfit between extracted γ and γ' phases was zero for alloys A and G.

(vi) It was not possible to calculate the long range order parameter of γ' because the intensity of the superlattice lines was not significantly different from the background radiation.

(vii) The error in titanium determination was ±0.2 at.%. This was larger than the intervals between the alloy compositions (table 1.2). Consequently, only alloys A, D and G were studied. These three alloys have identical compositions except for the systematic change in Ti.

(viii) All specimens used for the determination of APB and SSF energies were homogenised for 36 hours at 1570K, treated to grow the γ'

for 16 hours at 1390K and air cooled. This heat treatment produced an acceptably homogeneous product of γ' cubes in a γ matrix. After heat treatment all three alloys had the same volume fraction of γ' ($\sim$0.6) and the same γ' size. No misfit was measured so it was assumed that the misfit strengthening was negligible.

By heat treating in this way, any contributions to alloy strengthening by factors (ii) to (iv) of 1.5.3 will be constant.

CHAPTER 3

EXPERIMENTAL TECHNIQUES: DISLOCATION GENERATION AND OBSERVATION

3.1 Introduction

The aim of this investigation was to measure accurate values for the superlattice stacking fault (SSF) and anti-phase boundary (APB) energies of γ'. These energies are functions of state and as such are independent of the method by which defects are generated. A process of cold deformation and annealing has been used to produce extended superdislocation nodes (super nodes) and superdislocation networks, where the extended nodes contain superlattice stacking faults; these dislocation configurations allow simultaneous determination of stacking fault and APB energies. This chapter describes the deformation and annealing process used to create suitable defects. It then reviews the electron microscopical methods used to analyse these defects and describes the way in which they were applied in this investigation.

3.2 Dislocation and Defect Generation

Prior to deformation, samples of each of the as-cast alloys were heat treated in accordance with the conclusions of chapter 2.

Dislocations were introduced into the material by room temperature compression to between 1 and 2% strain by a stress of 400MPa. Specimens were deformed along the [001] axis. In this orientation the highest Schmidt factor lies in two directions on each of the (111), $(\bar{1}11)$, $(\bar{1}\bar{1}1)$ and $(1\bar{1}1)$ planes. Thus, eight intersecting slip systems are simultaneously active and these produce many intersecting dislocations on different planes (4.4).

After deformation the specimens were annealed for 24 hours at 1173K. At this temperature there was no change in the γ' size or structure

but dislocation climb was apparently possible allowing recovery to produce a more equilibrated dislocation structure.

3.3 Electron Microscopy

3.3.1 Thin specimen preparation

Thin foils for electron microscopy were manufactured from the deformed and annealed specimens. Three foil normals were studied: <001>, <110> and <111>. Specimens with the required orientations were obtained using the Laue back reflection technique with unfiltered tungsten radiation. First, the specimens were electro-polished for 15 secs. using Struers A1 electrolyte in a Struers Polectrol (voltage: 25V, flow rate: 2.5) before mounting them on a three-circle tilting goniometer. A Laue back reflection X-ray photograph of the polished surface was taken on Polaroid type 57 film. The specimen orientation was plotted onto a stereographic projection using a Greninger chart, as described by Cullity (1977). The specimen was then tilted to approximately the required orientation and a further Polaroid was taken to check the accuracy of the manipulation. If necessary, adjustments in orientation were made. The specimen was then carefully transferred to a fixed holder. Slices of material between 0.3 and 0.4mm thick were cut using a carborundum slitting disc. 3mm diameter blank discs were carefully stamped from the slices. These were ground down to between 0.13 and 0.2mm and profile electro-polished in a Fishione twin jet polisher or a Metalthin twin jet polisher containing a solution of 10% perchloric acid in ethanol at a temperature of between 268K and 273K, using a voltage of 30V and a current of approximately 70mA. The specimens were thoroughly washed in ethanol. The profiled blanks were polished to perforation using the equipment shown in figure 3.1. A solution of 20% perchloric acid in ethanol was used at 275K with a voltage of 10V and a current of 50mA. Polishing was stopped when the foil perforated and the hole was seen to grow rapidly. The specimen was again thoroughly washed in

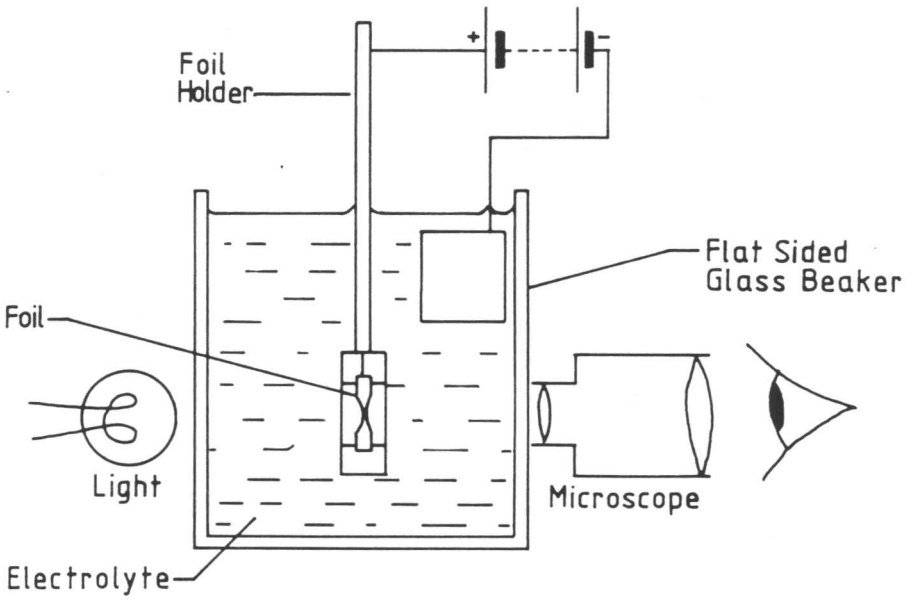

Fig. 3.1. Schematic illustration of the apparatus used for final polishing and perforation of foils.

ethanol. Specimens were stored in specimen boxes in a vacuum desiccator. Foils stored in this way lasted for up to three months.

3.3.2 Examination of thin specimens

All the transmission electron microscopy (TEM) reported in this thesis has been carried out on either a Philips 400T operating at 120kV ($\lambda = 3.35 \times 10^{-3}$nm) or a JEOL 200CX operating at 200kV ($\lambda = 2.51 \times 10^{-3}$nm). In addition to the conventional bright field technique, centred weak beam dark field imaging has also been extensively used. A detailed discussion of dynamical electron diffraction theory has not been undertaken.

3.3.3 Dislocation images in the electron microscope

Bright field dislocation images occur because the defect introduces a phase factor relative to the perfect lattice at the distorted planes around the core. This results in a broad dark line which represents the position of the dislocation but does not coincide with the core position. If the dislocation is viewed using a reflection from undistorted planes no image will result (3.3.5). Information which can be most easily interpreted is gained from the TEM image if diffraction is limited to one set of planes. This is done by tilting the foil so only one reciprocal lattice point is excited. Images formed in this condition are bright field two-beam conditions (fig. 3.2a) and the diffraction vector from (000) to (hkℓ), $\underline{g}$, describes the image. Bright field image contrast is improved if a slight positive deviation, $\underline{s}$, from the Bragg condition is applied (Hirsch, Howie, Nicholson, Pashley and Whelan, 1977 and fig. 3.2b). The sign and size of $\underline{s}$ can be measured as described in 3.3.4.

Under bright field conditions, with $\underline{s}$ close to zero, many planes around the dislocation are strongly diffracting; this gives rise to a low resolution dislocation image. If the diffracted beam is tilted so that it passes down the optic axis of the microscope (fig. 3.2c), the image is formed only by diffracted electrons. This is a centred dark field image;

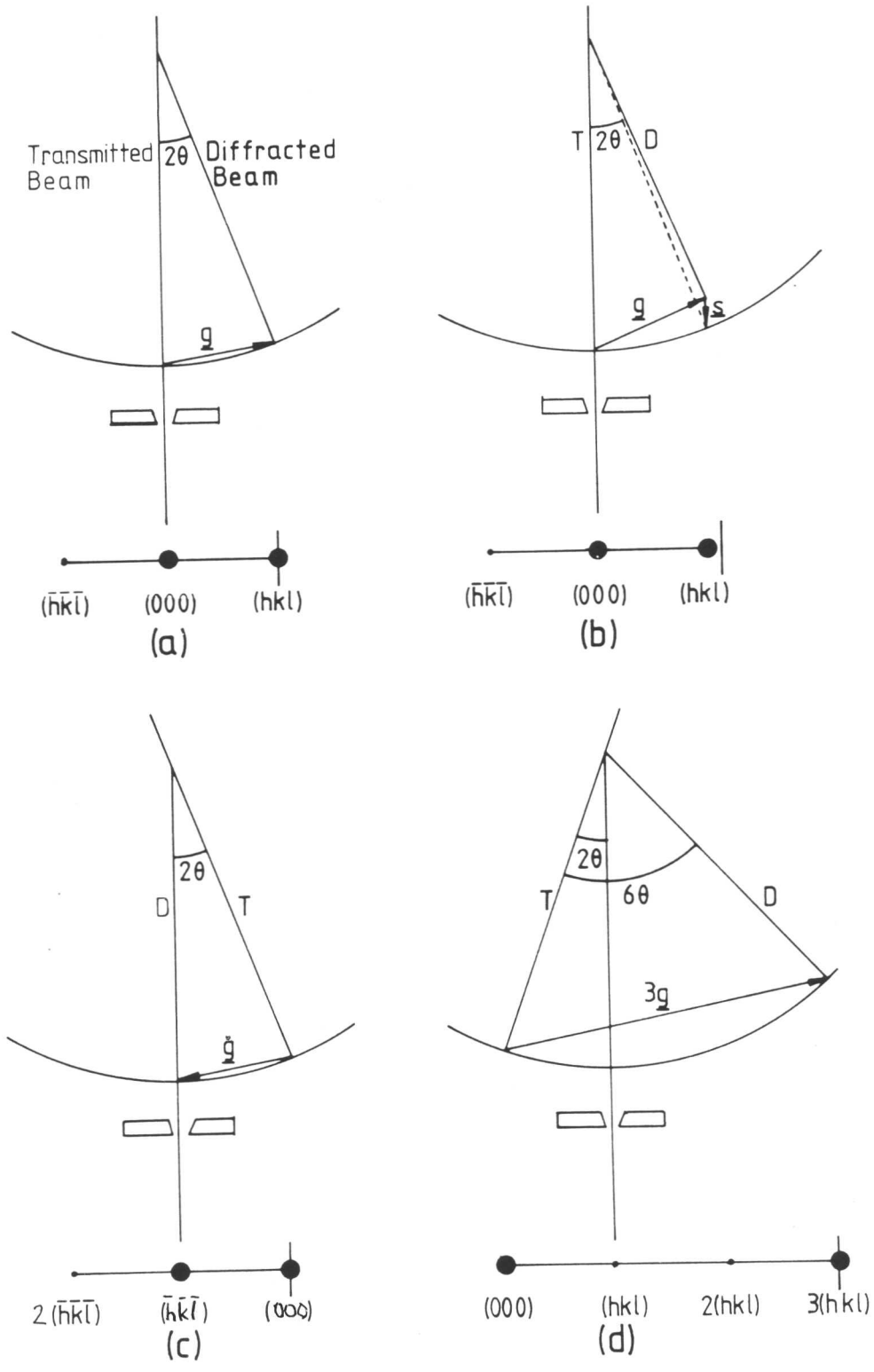

Fig. 3.2. Ray diagrams and Ewald sphere constructions showing conventional two-beam bright field in the Bragg condition (a), conventional two-beam bright field with a positive deviation from the Bragg condition (b), two-beam centred dark field (c), and ($\underline{g}$,$3\underline{g}$) weak beam dark field (d).

maximum intensity is gained when $\underline{s} = 0$.

An increase in resolution and contrast can be gained by forming centred dark field images from weak beams (fig. 3.2d), rather than the strong beams used for bright field and dark field. This is the weak beam technique (Cockayne, Ray and Whelan, 1969) and it is useful because the image is formed from the strongly distorted planes near the dislocation core which are in an orientation which diffracts strongly. In weak beam, dislocations appear as very narrow bright lines against a low intensity background. Cockayne et al. (1969) have shown that as $\underline{s}$ is increased, the width of the dislocation image is decreased and closer to the true position of the dislocation core.

Weak beam images are most easily produced following the method described by Howie and Sworn (1970). Their method, known as the $3\underline{g}$ weak beam technique, requires the bright diffracted spot of a normal two-beam condition to be tilted to the optic axis of the microscope to produce the configuration shown in figure 3.3. This method is preferred to that of Cockayne et al. (1969) because it provides more accurate positioning of defects and also allows switching between bright field and weak beam images; a useful aid to focusing the often very faint weak beam images. If a weak beam image from a higher order reflection is required, the specimen can be tilted so that the $n\underline{g}$ Kikuchi line intersects the $n\underline{g}$ diffraction spot (fig. 3.4a) or the next diffraction spot can be tilted to the optic axis of the microscope (fig. 3.4b). Throughout this thesis weak beam diffraction conditions will be reported as $W_{(n\underline{g},\ n\underline{g})}$. The first $n\underline{g}$ refers to the imaging spot, while the second $n\underline{g}$ refers to the strongly excited diffraction spot. Care must be taken in weak beam conditions because when $\underline{s}_{3\underline{g}} = 0$, in certain cases double images are formed from single dislocations. These can be misinterpreted as a single dislocation dissociated into two partials. However, Stobbs and Sworn (1971) showed that when $\underline{s}$ is made slightly positive of the $3\underline{g}$ reciprocal lattice point single

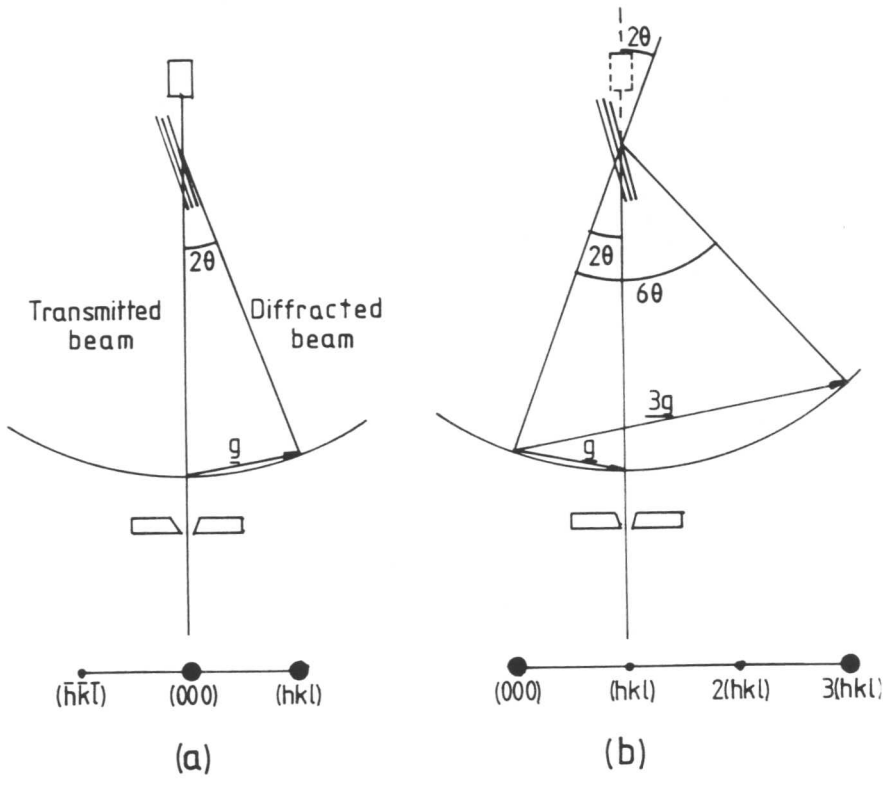

Fig. 3.3. Ray diagrams showing conventional two-beam bright field (a) and two-beam $W_{(\underline{g},3\underline{g})}$ weak beam dark field. If the gun is tilted to bring $(\bar{h}k\ell)$ in (a) to the centre as in (c), the diffraction condition is changed to produce the $W_{(\underline{g},3\underline{g})}$ weak beam dark field condition.

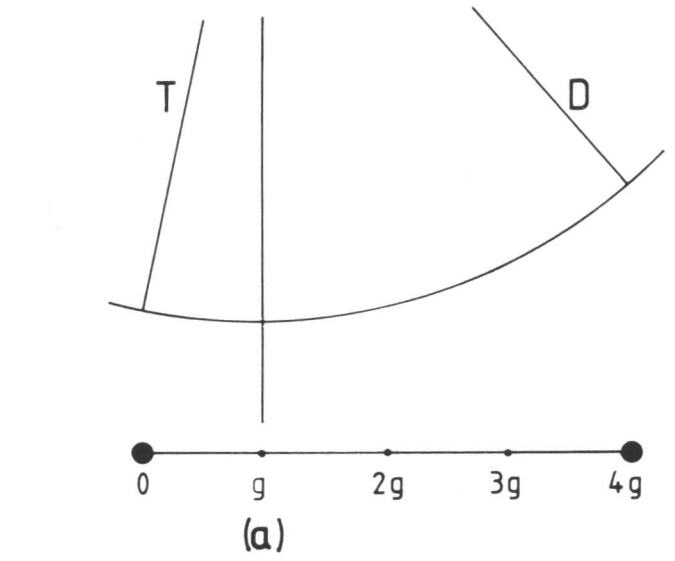

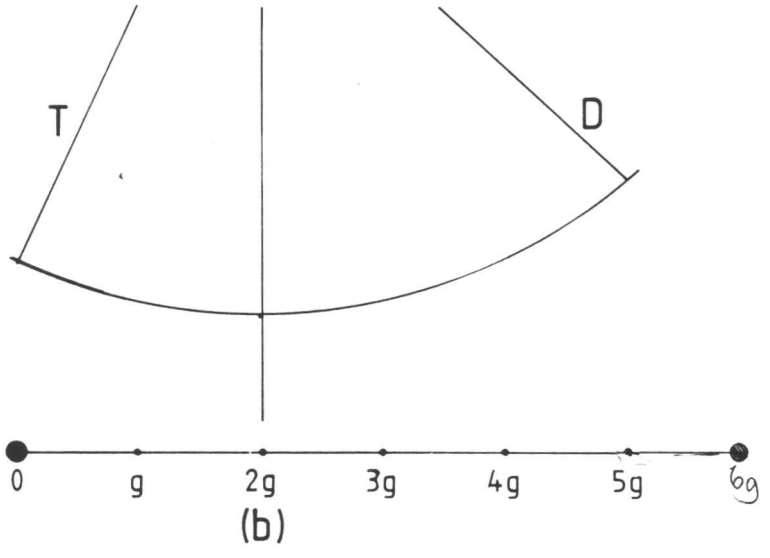

Fig. 3.4. Two possible diffraction conditions which can be used to obtain high values of $|\underline{s}|$: the $W_{(\underline{g},4\underline{g})}$ weak beam dark field condition (a), and the $W_{(2\underline{g},5\underline{g})}$ weak beam dark field condition (b).

dislocations always produce single images. To avoid this difficulty all weak beam micrographs presented were recorded with $\underline{s}$ slightly positive of the $3\underline{g}$ reciprocal lattice point. Care was always taken to ensure that no unwanted beams were excited during the tilting operation.

There are other dangers inherent in the quantitative interpretation of weak beam micrographs, particularly in thin areas and near specimen surfaces. These have been discussed by Stobbs and Sworn (1971) and Stobbs (1973). These papers suggest that reliable dislocation spacings may be obtained from centrally placed defects in foils greater than 70nm thick.

Cockayne et al. (1969) show from theory and by example that the intensity, and less strongly the position, of the peaks in sufficiently weak beam images from partial dislocations depends upon various factors; most critically on the depth of the dislocation in the foil. Cockayne (1973) shows by computation that the change in image with depth is a dynamical effect.

Cockayne also reported that the presence of a stacking fault or APB between paired dislocations may reduce the contrast of one of the pair. Experimentally these variations may lead to the disappearance of one of the dislocation images. If such a disappearance causes difficulties, a second image with a slight change in $\underline{s}$ can be used to overcome the difficulty. Reduction in the intensity of one image has frequently been observed during this investigation (eg. fig. 4.24b), probably due to a combination of the presence of a fault and a difference in dislocation depth.

3.3.4 Application of the weak beam technique to γ'

Cockayne (1973) has defined true weak beam conditions as those in which $|\underline{s}| > 2.0\times10^{-3}\text{nm}^{-1}$ (for $\underline{g}.\underline{b}\leq 2$) and $|\omega| = |\underline{s}\xi_{\underline{g}}| \geq 5$ with no other reflection excited. Under these conditions a dislocation image will be within 2nm of its core, it will have a half peak height width of $\sim$1.5nm and its position will vary by $<\pm 0.5$nm with depth in the foil.

To check that these conditions are satisfied the deviation parameter, $\underline{s}$, can be calculated from:

$$|\underline{s}| = \frac{(n-1)|\underline{g}|^2\lambda}{2} \qquad \text{eqn. 3.1}$$

where n is the excited reflection which need not be integral, $|\underline{g}|$ is the modulus of the diffraction vector and λ is the wavelength of the electrons. This formula can be geometrically derived from figure 3.2(a) and can be applied equally well to any diffracting condition.

The γ' precipitate in the alloys studied has a fairly large lattice parameter, $\underline{a}$ = 0.358nm (2.7), consequently $\underline{g}$ is fairly small. Using extinction distance data calculated, for an alloy similar to those studied here, by Oblak and Kear (1972) (table 3.1), values for $\underline{s}$ and ω have been calculated. It was found that at 120 kV true weak beam conditions were obtained for $\underline{g}$ = {111} and {200} when $W_{(\underline{g},5\underline{g})}$ conditions were satisfied for $\underline{g}$ = {220} and {311} $W_{(\underline{g},3\underline{g})}$ was found to be adequate. Thus good weak beam images were obtainable from all four of the commonly used $\underline{g}$ vectors. For 200 kV the $W_{(\underline{g},4\underline{g})}$ condition was sufficient for $\underline{g}$ = {220} and {311}, but $\underline{g}$ = {111} and {200} required a prohibitively large reflection to be excited for true weak beam conditions to be obtained.

It is worth remembering that although $\underline{s} = 2.0\times10^{-3}nm^{-1}$ is the lower limit for accurate quantitative weak beam microscopy near weak beam conditions using large deviation parameters less than $2.0\times10^{-3}nm^{-1}$ can be very useful in improving the contrast and resolution at complex dislocation interactions. Both true and near weak beam conditions have been extensively employed to aid the identification of dislocation types and the interpretation of complicated dislocation interactions.

The weak beam dark field technique is an invaluable aid to the kind of quantitative microscopy required for an investigation of this type. It enables more accurate determination of dislocation spacings and positions than bright field imaging and it therefore allows more accurate values of

Table 3.1. Extinction Distances (in nm) for Selected Reflections in Mar-M 200 (table 1.1) after Oblak and Kear (1972)

Fundamental		Superlattice		
hkℓ	Extinction distance	hkℓ	Extinction distance	Effective extinction distance
111	34	100	1547	700
200	39	110	30614	-
220	57	300	1748	5880
311	70			

Table 3.2. Summary of $\underline{g}.\underline{b}$ Values for Partial Dislocations

$\underline{g}.\underline{b}$	ω $(\underline{s}.\xi_{\underline{g}})$	Comment	Reference
0	ALL	INVISIBLE	Howie & Whelan (1961) Silcock & Tunstall (1964)
± 1	$\omega \lesssim 1$	VISIBLE	
$\pm\frac{1}{3}$	$1<\omega<1$	INVISIBLE N.B SF in contrast	Howie & Whelan (1962) Clarebrough & Morton (1969)
$\pm\frac{2}{3}$	$\omega<0.7$	VISIBLE	
$*-\frac{2}{3}$	$\omega \gtrsim 0.7$	VISIBLE	Silcock & Tunstall (1964)
$*+\frac{2}{3}$	$\omega \gtrsim 0.7$	INVISIBLE	
$*-\frac{4}{3}$	$\omega \gtrsim 0.7$	INVISIBLE	Oblak & Kear (1972)
$*+\frac{4}{3}$	$\omega \gtrsim 0.7$	VISIBLE	

* Table constructed with the fault to RIGHT of dislocation line; if the fault is to the LEFT the signs are reversed.

stacking fault energies and APB energies to be calculated (chapter 5). The technique has been applied to many alloy systems to determine stacking fault energies: for example in Cu-Al (Cockayne et al., 1969), in Si (Ray and Cockayne, 1970), in Ag (Cockayne, Jenkins and Ray, 1971), in Cu (Stobbs and Sworn, 1971) and in austenitic stainless steel (Bampton, Jones and Loretto, 1978). APB energies in ordered structures have been determined in Fe-3% Al by Ray, Crawford and Cockayne (1970), in Ll_2 structures, Zr_3Al (Howe, Rainville and Schulson, 1974) and Ni_3Ga (Suzuki, Ichihara and Takeuchi, 1979). The technique has also been employed to observe complex dislocation interactions, for example, Ray and Cockayne (1971) observed nodes in silicon.

3.3.5 Burgers vector analysis of $a/_2$<110> dislocations

This section discusses the use of the $\underline{g}.\underline{b} = 0$ and $\underline{g}.\underline{b}\times\underline{u} = 0$ invisibility criteria for the identification of $a/_2$<110> dislocations. The theoretical description of the contrast arising from crystal defects such as dislocations and stacking faults has been formulated by Howie and Whelan (1961) and is contained in the Howie-Whelan equations. These equations may be represented in many ways but the most useful in this case is the one shown below.

In a two-beam dynamical diffraction condition the amplitudes of the transmitted (ϕ_o) and diffracted (ϕ_g) waves may be represented as:

$$\frac{d\phi_o}{dz} = \frac{i\pi\phi_o}{\xi_o} + \frac{i\pi\phi_g}{\xi_g}\exp(2\pi i\underline{s}z+2\pi i\underline{g}.\underline{R}) \qquad \text{eqn. 3.2a}$$

and

$$\frac{d\phi_g}{dz} = \frac{i\pi\phi_o}{\xi_g}\exp(-2\pi i\underline{s}z-2\pi i\underline{g}.\underline{R}) + \frac{i\pi\phi_g}{\xi_o} \qquad \text{eqn. 3.2b}$$

where $\underline{s}$ is the deviation vector, ξ_g is the extinction distance, $\underline{g}$ is the diffraction vector, $\underline{R}$ is the defect displacement vector, i is $\sqrt{-1}$, and z is the distance of the defect from the top surface of the foil, as shown

in figure 3.5. Effectively, these equations mean that distortion of the lattice creates a phase factor $\exp(-i\alpha)$ where $\alpha=2\pi\underline{g}.\underline{R}$. This phase factor is superimposed on the normal crystal scattering. So, if an atom is displaced by $\underline{R}$, then the phase of the scattered wave is changed by $\exp(-2\pi i\underline{g}.\underline{R})$. This phase factor represents the scattering from the diffracted to the transmitted beam as $\exp(2\pi i\underline{g}.\underline{R})$ while the reverse is $\exp(-2\pi i\underline{g}.\underline{R})$. Thus, in a bright field image, as stated in 3.3.3, the strain field will diffract electrons away and appear darker.

Hirsh et al. (1977) have shown that for an edge dislocation in an isotropic medium:

$$\underline{R} = \frac{1}{2\pi}\left[\underline{b}\Phi+\underline{b}\ \frac{\sin 2\Phi}{4(1-\nu)}+(\underline{b}\times\underline{u})\left[\frac{(1-2\nu)}{2(1-\nu)}\ln r+\frac{\cos 2\Phi}{4(1-\nu)}\right]\right] \qquad \text{eqn. 3.3}$$

where $\underline{b}$ is the dislocation Burgers vector,

, $\underline{u}$ is a unit vector in the positive direction of the dislocation line, ν is Poissons ratio, r is a radial co-ordinate measured from the dislocation and Φ is an angular co-ordinate in the plane normal to the line measured from the slip plane (fig. 3.5). The definition of $\underline{b}$ is consistent with the definition of Bilby, Bullough and Smith (1955) more commonly known as the FS/RH perfect crystal convention (fig. 3.6).

Now, if the crystal is orientated such that the beam 'sees' no distortion (i.e. the dislocation cannot be seen by an incoming beam) the phase factor, α, must be zero, so $\underline{g}.\underline{R}=0$. If eqn. 3.3 is multiplied through by $\underline{g}$ and equated to zero, it is seen that the condition for the invisibility of a general dislocation is when $\underline{g}.\underline{b}$, $\underline{g}.\underline{b}_e$ and $\underline{g}.\underline{b}\times\underline{u}$ are all zero.

This is the basis for the determination of $a/_2\langle 110\rangle$ dislocation

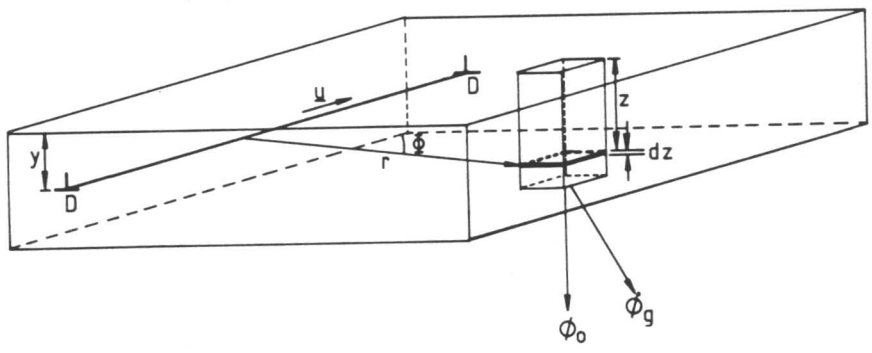

Fig. 3.5. The column approximation for a thin foil containing a dislocation DD. This approximation is used to produce equations 3.2 and 3.3. See text for details.

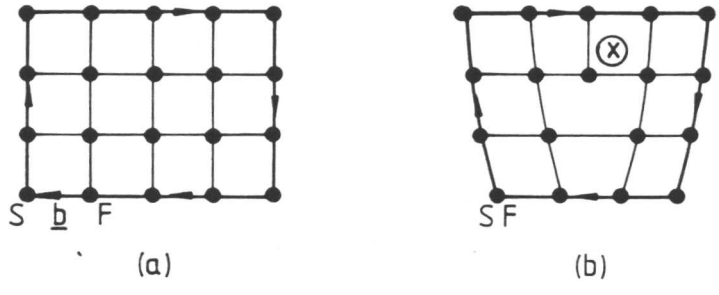

Fig. 3.6. A Burgers circuit around a dislocation (b) does not close in the perfect lattice without the introduction of a vector equal to the Burgers vector (a). The criterion used for Burgers vector determination is the FS/RH criterion.

Burgers vectors in isotropic materials because $\underline{g}\cdot\underline{b}$ is either zero, when the reflection used is for undistorted plane, or an integer, when the reflection used comes from distorted planes. When $\underline{g}\cdot\underline{b}=0$ the dislocation is invisible and it is visible when $\underline{g}\cdot\underline{b}$ is an integer. This method is equally applicable to weak beam as well as bright field conditions.

By recording a series of bright field or weak beam micrographs in various two beam conditions the identity and type of any $a/_2\langle 110\rangle$ dislocation can be obtained. In this investigation the commonly used diffraction vectors were {111}, {200}, {220} and {311}. In all cases $\underline{s}$ was positive.

Many dislocation analyses have been undertaken using the technique described above and these are presented in subsequent chapters.

3.3.6 Burgers vector analysis of $a/_6\langle 211\rangle$ and $a/_3\langle 211\rangle$ dislocations

The determination of the Burgers vectors of $a/_6\langle 211\rangle$ and $a/_3\langle 211\rangle$ dislocations in γ' is rather more complex than that for $a/_2\langle 110\rangle$ dislocations discussed above because the $\underline{g}\cdot\underline{b}$ values are not necessarily integral. Some general rules for identification have been set out using image simulation techniques. Unfortunately, these have some associated anomalies which cannot be explained adequately and the rules must, therefore, be applied with discretion. Each of the possible $\underline{g}\cdot\underline{b}$ values is discussed individually below.

As above, when $\underline{g}\cdot\underline{b}=0$ dislocations are invisible and when $\underline{g}\cdot\underline{b}$ is an integer they are visible for all values of $\underline{s}$ and ω (Howie and Whelan, 1961 and Silcock and Tunstall, 1964).

When $\underline{g}\cdot\underline{b}=\pm\frac{1}{3}$ it is generally accepted that when $\omega\lesssim 1$ all $a/_3\langle 211\rangle$ and $a/_6\langle 211\rangle$ dislocations are invisible; this also appears to hold for values of ω above one (Howie and Whelan, 1962, Clarebrough and Morton, 1969a,b and Clarebrough, 1971). However, Clarebrough and Morton (1969a,b) have reported that strong contrast can arise from Frank partial dislocations when

particular beam directions are employed and it is clearly possible that other anomalies could exist.

When $\underline{g}.\underline{b}=\pm\frac{2}{3}$ the situation is more complex as the position of the stacking fault associated with the partial dislocation is important, except for $\omega\lesssim 0.7$ where the dislocation will be visible for $\pm\frac{2}{3}$. According to Silcock and Tunstall (1964) when $\omega\gtrsim 0.7$ and the fault lies to the right of the dislocation, when $\underline{g}.\underline{b}=-\frac{2}{3}$ a dislocation is visible and when $\underline{g}.\underline{b}=+\frac{2}{3}$ a dislocation is invisible. Again this rule is not correct in all cases.

The final condition to be considered is $\underline{g}.\underline{b}=\pm\frac{4}{3}$. Only a small amount of work has been performed at this condition. Using a combination of computation and practical observation Oblak and Kear (1972) have found that for $\omega\gtrsim 0.7$ with the fault lying to the right of the dislocation line when $\underline{g}.\underline{b}=-\frac{4}{3}$ the dislocation was invisible and when $\underline{g}.\underline{b}=+\frac{4}{3}$ the dislocation was visible.

If the dislocation sense, $\underline{u}$, is reversed then the $\pm\frac{2}{3}$ and $\pm\frac{4}{3}$ conditions will also be reversed. Table 3.2 summarises the invisibility criteria for $a/_3\langle 211\rangle$ and $a/_6\langle 211\rangle$ dislocations which have been applied throughout this investigation.

As in the case of $a/_2\langle 110\rangle$ dislocations a series of bright field and weak beam micrographs at various two beam conditions can unambiguously identify the Burgers vector and type of any $a/_3\langle 211\rangle$ or $a/_6\langle 211\rangle$ dislocations. Commonly used diffraction vectors were {111}, {200}, {220} and {311} with $\underline{s}$ positive. Since the reference system described above is based on the image seen on the microscope viewing screen all photo micrographs reproduced in this dissertation have been printed in that orientation.

3.3.7 The effect of crystal anisotropy on dislocation images

The equation for $\underline{R}$ in an anisotropic medium is considerably more complex than equation 3.3. A detailed derivation can be found in the papers of Eshelby, Read and Shockley (1953) and Stroh (1958). Head, Humble,

Clarebrough, Morton and Forwood (1973) have shown that in certain cases, which correspond to elastic isotropy, the invisibility criteria hold but that in many anisotropic crystals dislocation invisibility when $\underline{g}\cdot\underline{b}=0$ only occurs due to the weak contrast in this condition. Many papers have been written stating that for high diffraction vectors, e.g. {311}, {301}, {420} some dislocations will be invisible when $\underline{g}\cdot\underline{b}\neq 0$, e.g. France and Loretto (1968) and Loretto and France (1969a,b). Oblak and Rand (1972) have shown that in Ni_3Al $\underline{g}\cdot\underline{b}=2$ and $\underline{g}\cdot\underline{b}=4$ give dislocation invisibility in certain conditions.

Despite the results of these papers and the fact that the anisotropy factor of the γ' in the alloys studied is 2.7 (see 6.2.1), the application of the effective invisibility criteria has always given self-consistent results. Other investigations of superalloy microstructures such as those reviewed by Kear (1974) have also given self-consistent results by applying the same criteria. All the dislocation analyses presented here have been carried out without the aid of image contrast computation.

3.3.8 Dislocation image position with respect to the line sense

The position of a dislocation image with respect to the actual dislocation line is dependant upon the value of $\underline{g}$ and $\underline{s}$. It will always lie to a given side of the true dislocation line for a given $\underline{s}$ and on different sides of the dislocation line for $+\underline{g}$ and $-\underline{g}$ (fig.3.7 and Hirsch et al., 1977).

If two bright field micrographs are taken, one at $+\underline{g}$ and one at $-\underline{g}$, then the dislocation line position can be defined and, provided $\underline{g}$ and $\underline{s}$ are also known, then, following the FS/RH system, the sense of the dislocation Burgers vector can be determined unambiguously.

The switch in dislocation image position when $\underline{g}$ is reversed can also be used to study dislocation pairs. In the gamma prime phase of superalloys two types of dislocation pairs are observed: the dipole (two dislocations of opposite sign on different planes) and the superdislocation

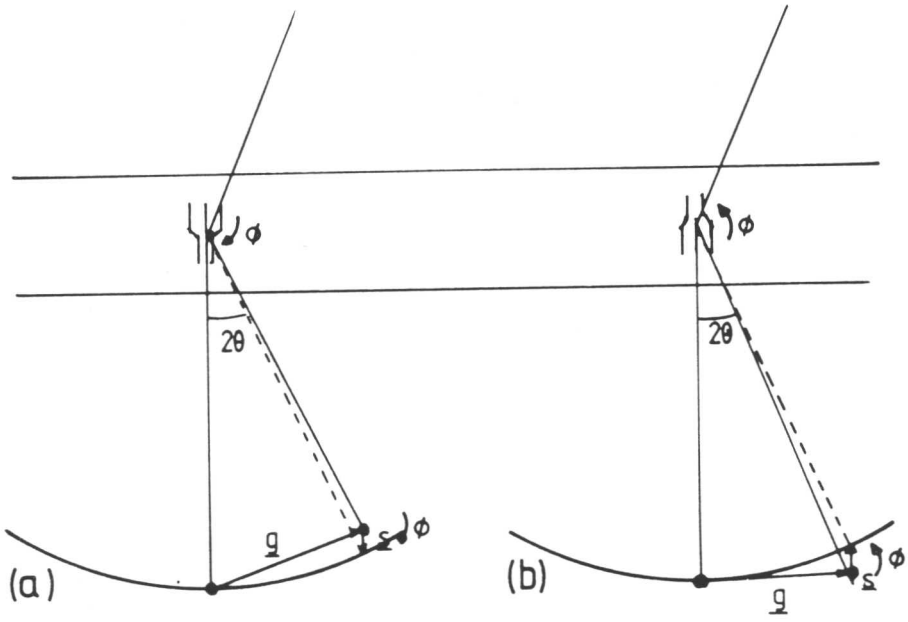

Fig. 3.7. Illustration showing that a dislocation locally tilts the reflecting planes to produce a positive deviation from the Bragg condition (a). An identical inverted dislocation in the same diffracting conditions tilts the reflecting planes to produce a negative deviation from the Bragg condition (b). The images must therefore be to one side of the dislocation line.